
Electronic Thesis and Dissertation Repository

8-19-2014 12:00 AM

Fully Automated Segmentation and Quantification of Abdominal Adipose Tissue Compartments in Mouse MRI

Colin M. McCurdy
The University of Western Ontario

Supervisor
Charles McKenzie
The University of Western Ontario

Graduate Program in Medical Biophysics

A thesis submitted in partial fulfillment of the requirements for the degree in Master of Science

© Colin M. McCurdy 2014

Follow this and additional works at: <https://ir.lib.uwo.ca/etd>



Part of the [Medical Biophysics Commons](#)

Recommended Citation

McCurdy, Colin M., "Fully Automated Segmentation and Quantification of Abdominal Adipose Tissue Compartments in Mouse MRI" (2014). *Electronic Thesis and Dissertation Repository*. 2366.

<https://ir.lib.uwo.ca/etd/2366>

This Dissertation/Thesis is brought to you for free and open access by Scholarship@Western. It has been accepted for inclusion in Electronic Thesis and Dissertation Repository by an authorized administrator of Scholarship@Western. For more information, please contact wlsadmin@uwo.ca.

FULLY AUTOMATED SEGMENTATION AND QUANTIFICATION OF
ABDOMINAL ADIPOSE TISSUE COMPARTMENTS IN MOUSE MRI

(Integrated Article)

by

Colin Matthew McCurdy

Graduate Program in Medical Biophysics

A thesis submitted in partial fulfillment
of the requirements for the degree of
Master of Science

The School of Graduate and Postdoctoral Studies
The University of Western Ontario
London, Ontario, Canada

© Colin McCurdy 2014

Abstract

Obesity currently affects 25% of Canadians and is strongly associated with many diseases including diabetes, cardiovascular disease, and cancer. However, only Intra-Abdominal Adipose Tissue (IAAT) is an important predictor of obesity associated disease and mortality. Magnetic Resonance Imaging (MRI) is an effective modality for imaging fat and methods have been developed to automate segmentation of IAAT. Currently existing techniques for automated segmentation in mice require acquisition using high magnetic field MRI equipment and use image acquisition techniques with low precision for fat quantification. We demonstrate a new fully automated technique for fat quantification in clinical strength mouse MRI through adaptation of an existing human fat quantification technique. We validated this method using images collected from mice in a 3 T clinical MRI against manual segmentation. Dice correlation coefficients revealed that 84% of voxels agreed for Subcutaneous Adipose Tissue (SAT) and 87% of voxels agreed for IAAT.

Keywords

Magnetic Resonance Imaging (MRI), Obesity, Intra-Abdominal Adipose Tissue (IAAT), Subcutaneous Adipose Tissue (SAT), Automated Segmentation, Adipose Quantification, Iterative Decomposition of water and fat with Echo Asymmetry and Least-squares estimation (IDEAL), Water-fat Imaging

Co-Authorship Statement

The work in chapter 2 entitled “Validation of Volumetric MRI Adipose Analysis on Mice Using a Fully Automated Segmentation Method” is in preparation to be submitted to the Journal of Magnetic Resonance Imaging and is co-authored by Colin McCurdy, Bryan Addeman, Curtis Wiens, Lanette Friesen-Waldner, Trevor Wade, Abraam Soliman, Kevin Sinclair, Jacqueline Harris, and Charles McKenzie. Colin McCurdy was responsible for adaptation of the code, acquisition of in vivo images, optimization of automated segmentation, manual segmentation of images, analysis of automated segmentation technique, and writing of the manuscript. Bryan Addeman wrote the original AdipoQuant code that was adapted for this project and advised about validation of the technique. Curtis Wiens and Trevor Wade acquired some of the in vivo images. Lanette Friesen-Waldner and Jacqueline Harris assisted through anesthetizing and handling animals for the experiments. Abraam Soliman assisted with reconstruction of images that could not be reconstructed with the MRI software through the use of MaxIDEAL. Curtis Wiens, Lanette Friesen-Waldner, Trevor Wade, Kevin Sinclair, and Jacqueline Harris all assisted in the set up and takedown of equipment for experiments. Charles McKenzie provided advice regarding experiment procedures and validation of the technique and with Lanette Friesen-Waldner assisted in the preparations of the manuscript.

Acknowledgments

First off, I would like to acknowledge my supervisor Dr. Charles McKenzie. His ability to convey knowledge was critical to advancing my understanding of MRI Physics and the techniques used in this thesis. In addition, the environment he has created in our lab is amazing for productivity and communication – whether it be academic or otherwise. I am very grateful for the opportunity to work under his guidance and within this environment. Secondly, I would like to thank Lanette Friesen-Waldner. Her efforts in organizing and performing a majority of the experiments within our lab were greatly appreciated. I would also like to thank Bryan Addeman for his assistance in navigating his code, as well as his help in determining where some of my problems in adapting his code were originating. The extra effort put forward by Abraam Soliman to always ensure my images were promptly reconstructed when there was an error with the GE online recons was greatly appreciated as well. In addition, I am thankful to all of the remaining members of the McKenzie lab for their assistance in numerous different tasks.

Lastly I would like to thank my parents, Christopher and Terry McCurdy, and my fiancée, Nicolette Burchell. You have been extremely supportive of my work and I'm grateful for all of your assistance throughout my degree.

Table of Contents

Abstract	ii
Co-Authorship Statement.....	iii
Acknowledgments.....	iv
Table of Contents	v
List of Tables	viii
List of Figures	ix
List of Abbreviations	xi
1 Introduction	1
1.1 Fat Distribution and Disease.....	1
1.1.1 Obesity related disease.....	1
1.1.2 Current tests for fat distribution and disease.....	7
1.1.3 Rodent Research	10
1.2 MR Physics	11
1.2.1 Nuclear Magnetic Resonance and MRI Basics.....	11
1.2.2 Net Magnetization within a Magnetic Field	13
1.2.3 Magnetization Relaxation	15
1.2.4 Resolution and Gradients	17
1.2.5 Water-Fat Imaging.....	20
1.2.6 Water and Fat Imaging Techniques	21
1.3 Fat Segmentation	26
1.3.1 Mouse Anatomy.....	27
1.3.2 Rodent segmentation techniques.....	28
1.3.3 Limitations of current techniques	30

1.3.4	Proposed Solutions / Thesis Objectives	32
2	Validation of Volumetric MRI Adipose Analysis on Mice Using a Fully Automated Segmentation Method	34
2.1	Introduction.....	34
2.2	Methods.....	36
2.2.1	MRI Acquisition	36
2.2.2	Automated Segmentation.....	36
2.2.3	Segmentation Analysis.....	44
2.2.4	Reproducibility	44
2.2.5	Statistical Analysis.....	44
	Results	46
2.3	Discussion	48
2.4	Conclusion	51
3	Conclusion	52
3.1	Summary of Findings.....	52
3.1.1	Rapid Analysis of Full Abdominal Volumes.....	52
3.1.2	Agreement Between Segmentation Techniques	52
3.1.3	Reproducibility	53
3.1.4	Transferability.....	53
3.2	Future Work	54
3.2.1	Disease onset from Obesity	54
3.2.2	Expansion to Other Rodents	54
3.2.3	Rodent Pregnancy	55
3.3	Conclusion	55
4	References	56
5	Ethics Approval.....	61

6 Curriculum Vitae.....	62
-------------------------	----

List of Tables

Table 1.1 BMI Classification.....	7
-----------------------------------	---

List of Figures

Figure 1.1 Obesity rates in Canadian Provinces	2
Figure 1.2 Increasing costs of Obesity in Canada.....	3
Figure 1.3 Mortality Rates and Aging with Diabetes	4
Figure 1.4 Adipose Tissue Deposits in Humans	6
Figure 1.5 Adiposity in Spinal Regions	9
Figure 1.6 Effect of Magnetic Field on Magnetic Moments of Nuclei	12
Figure 1.7 Net Magnetization of Nuclei in a Magnetic Field	14
Figure 1.8 Dephasing of Transverse Magnetization	16
Figure 1.9 K-space and Image Space.....	19
Figure 1.10 Chemical Shift between Water and Fat	21
Figure 1.11 Effect of Field Inhomogeneity on Phases of Water and Fat.....	22
Figure 1.12 NSA for Three Point Dixon at Different Echo Times	24
Figure 1.13 Spectrum of ^1H in different Fat Species	26
Figure 1.14 Superficial Fascia in a Human MR Image	28
Figure 1.15 Differences in Anatomy	30
Figure 2.1 K-means on In Phase Image to Create an Image Mask.....	37
Figure 2.2 Adipose Tissue Mask Creation.....	38
Figure 2.3 Superficial Fascia in a Mouse MR Image	39

Figure 2.4 Water Mask and Polar Water Mask.....	40
Figure 2.5 Lowest Voxels in Polar Coordinates and Smoothing.....	41
Figure 2.6 Intra-Abdominal Cavity.....	42
Figure 2.7 3D Segmented Volume Images	42
Figure 2.8 Summary of Segmentation Process	43
Figure 2.9 Difference Image Between Manual and Automated Segmentations.....	46
Figure 2.10 Bland-Altman Plot for Subcutaneous Adipose Measurements	47
Figure 2.11 Bland-Altman Plot for Intra-Abdominal Adipose Measurements.....	48

List of Abbreviations

BA	Bland-Altman
CT	Computed Tomography
CV	Coefficient of Variation
CVD	Cardiovascular Disease
DC	Dice Coefficient
DM	Diabetes Mellitus
FOV	Field of View
IAAT	Intra-Abdominal Adipose Tissue
IDEAL	Iterative Decomposition of water and fat with Echo Asymmetry and Least-squares estimation
IP	In Phase
MR	Magnetic Resonance
MRI	Magnetic Resonance Imaging
NEX	Number of Excitations
NSA	Number of Signal Averages
OP	Out of Phase
RF	Radiofrequency
SAT	Subcutaneous Adipose Tissue
SNR	Signal to Noise Ratio
T	Tesla
TAT	Total Adipose Tissue
TE	Echo Time
TR	Repeat Time
VD _A	Average Volume Difference
WHR	Waist to Hip Ratio

1 Introduction

1.1 Fat Distribution and Disease

1.1.1 Obesity related disease

Obesity has become increasingly prevalent worldwide and is causing increasing costs for the support and care for obese patients. Obesity is defined as having excess body fat sufficient to adversely affect health and is caused by an imbalance between energy intake and expenditure. There are many factors that can cause this imbalance, but the most prevalent and problematic come from diet and amount of physical activity. About one quarter of Canadians are classified as obese according to measured height and weight data from 2007-2009¹. Across Canada obesity levels range from 18% to 36.7% of the province, as shown in Figure 1.1.

There is also a trend toward increasing obesity in Canada, particularly the worst cases of obesity based on Body Mass Index (BMI). BMI will be explained fully in Section 1.1.2, but is a measure of the adiposity of patients based on their height and weight. There has been a massive 3 fold increase in the most obese patients². The trend of increasing obesity is not only in adults, but also in children with 8.6% of children aged 6-17 being classified as obese. In 1981, obesity in adults was approximately half of current reported values³. This is not only a problem in Canada, as over 1 billion adults worldwide are classified as overweight, with an additional 300 million being classified as obese⁴. The increases in obesity worldwide are expected to continue to rise substantially through 2019⁵.

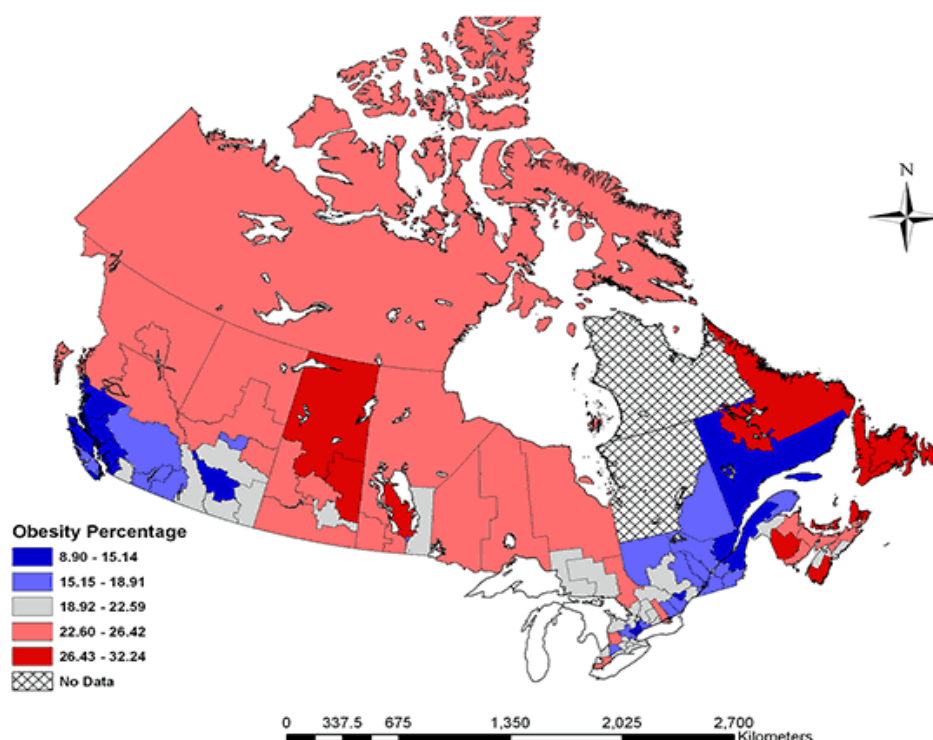


Figure 1.1 Obesity rates in Canadian Provinces

Map of Canada with regions coloured based on percentage of the province classified as obese. Some data from Quebec was not available. [Image From: Slater J *et al.* 2009⁶]

Higher levels of obesity are very problematic due to the expensive and chronic nature of the disease. It requires long-term care as it is linked to metabolic syndrome and its associated diseases such as diabetes, cardiovascular disease, and cancer⁷. The economic costs for obesity have been steadily increasing over time. The annual estimated cost in 2000 amounted to \$3.9 billion, but had risen to at least \$4.6 billion by 2008, and increase of \$700 million in just 8 years³ (see Figure 1.2). The 2008 estimates of obesity costs for Canada ranged from \$4.6 billion to \$7.1 billion^{3,8}, split between direct and indirect costs. The range results from the number of diseases considered caused by obesity, with the

lower estimate focusing on 8 chronic diseases. For the lower estimate, indirect costs were \$2.63 billion and are an estimate of the value of economic output lost from premature death or lost time from work. Direct costs were \$1.98 billion and included hospital care, drugs, physician care, and institutional care. With the costs and prevalence of obesity increasing, it is important to invest time and effort into researching obesity and its associated diseases to develop better care and prevention.

The most costly disease associated with obesity is diabetes, with over 9 million Canadians living with diabetes or pre-diabetes. Diabetes is a metabolic disease associated with consistent high levels of glucose in the blood. In normal patients, insulin will regulate the blood glucose levels so that after a spike in glucose (such as eating) the blood glucose levels will return to normal.

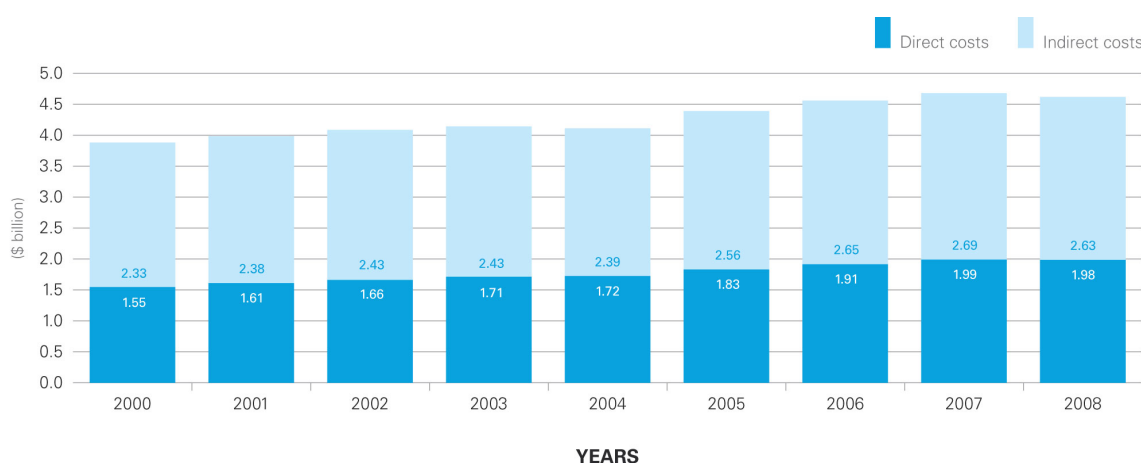


Figure 1.2 Increasing costs of Obesity in Canada

The increasing yearly costs of obesity in Canada displayed as a summation of the indirect and direct estimates. All of the costs were determined using 8 diseases strongly correlated to obesity. [Image From: Corscadden L *et al.* 2011³]

Insulin is a hormone produced in the pancreas that causes cells to uptake glucose from blood. In diabetic patients, high levels of glucose are not lowered due to insufficient insulin or the inability of the cells to respond to insulin properly. The deficiency of insulin and the inability of the insulin to reduce blood glucose levels are two different

types of diabetes. The first type, where insulin isn't being produced, is less common and caused mostly by genetic factors. The second type is much more prevalent with 90% of diabetes patients having the preventable Type 2 Diabetes Mellitus (DM). Type 2 DM is caused by excess adiposity resulting in the cells losing sensitivity to insulin. Lowered insulin production can also occur as the disease progresses. Becoming diabetic doubles your chances of early death, and diabetes is the 8th leading cause of death worldwide with 1.5 to 5.1 million deaths per year⁹. As seen in Figure 1.3, the mortality rates for individuals with diabetes increases as the patient's age, although the rate ratio is much higher at younger ages.

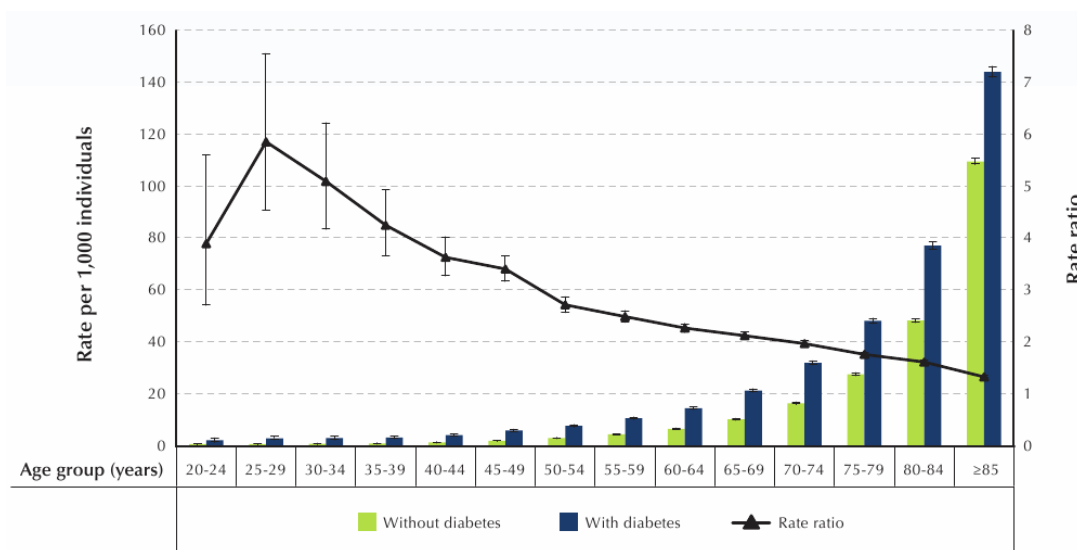


Figure 1.3 Mortality Rates and Aging with Diabetes

Analysis of mortality rates between both patients without diabetes and patients with diabetes based on age. The rate ratio was calculated to display the mortality risk of being diabetic vs. the normal mortality rate. Mortality rates for younger patients (20-39 yrs) with diabetes were over 4 times higher, whereas mortality rates for older patients (50+) were less than 3 times higher. [Image From: Petellier C *et al.* 2012¹⁰]

Because DM is preventable, research on this disease is important. Prevention and treatment revolve around returning to a normal weight, increasing physical exercise, and eating healthy. These are typically drastic lifestyle changes that ideally should occur prior

to diabetes diagnosis. Knowledge about disease progression and development are vitally important for determining when and how to prevent or treat these ailments.

Cardiovascular disease (CVD), another prominent ailment stemming from obesity, is an umbrella term for diseases affecting the heart or blood vessels. The principle cases included in this are coronary artery disease, vascular diseases in the kidney or brain, and peripheral artery disease. A majority of these diseases involve the buildup or movement of plaque in blood vessels resulting in impeded blood flow. Plaque is typically a buildup of macrophage cells or debris containing lipids and other material that impedes flow. Plaque buildup is strongly correlated with obesity, with recent research showing that obesity is associated with a 2.76 times higher incidence of non-calcified coronary artery plaque¹¹. Cardiovascular disease is currently the number one cause of death with 29.34% of deaths resulting from this disease. Although CVD is typically associated with the elderly, reports from a study encompassing 2000-2008 show that there are increasingly high risk factors for CVD in adolescents. Within the age groups of 12-19 years, the prevalence for pre-hypertension/hypertension was an astounding 14%¹². The unfortunate part of cardiovascular diseases is that the progression of the disease is not easy to research. Typically plaque buildups are very small and it is not easy to predict their location. Small plaque buildup is typically asymptomatic as well. Therefore the primary method for determining how to reduce the incidence of CVD is to study obesity and how the disease develops in obese or overweight patients.

Although several diseases are strongly correlated with obesity, weight measurements are not optimal for predicting disease onset or mortality. It has been found that the fat distribution in the body is a much better predictor of disease and mortality than total fat (or body weight)¹³⁻¹⁵. There are two major deposits of fat in the body: Subcutaneous Adipose Tissue (SAT) and Visceral or Intra-Abdominal Adipose Tissue (IAAT) as displayed in Figure 1.4.

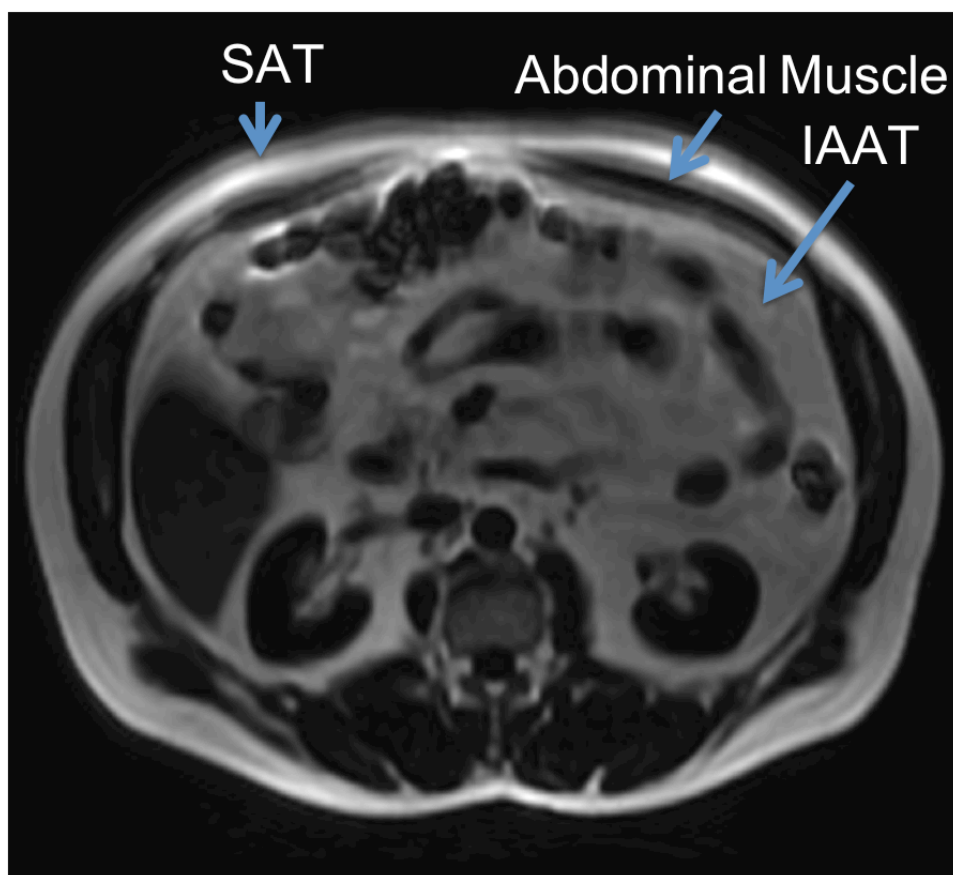


Figure 1.4 Adipose Tissue Deposits in Humans

Human axial MR image within the abdomen depicting the locations of the Intra-Abdominal Adipose Tissue (IAAT) and Subcutaneous Adipose Tissue (SAT). IAAT is located within the abdominal muscle layer surrounding organs and buildup of fat in this deposit results in a more apple-shaped figure. SAT is located beneath the skin and outside of the abdominal muscle layer and buildup of this deposit results in a more pear-shaped figure.

SAT is the fat deposit located just beneath the skin, and outside of the abdominal muscle layer. Similar to the Total Adipose Tissue (TAT), SAT is not predictive of disease or mortality. IAAT is a much better predictor of all of the obesity related diseases, and associated mortality. IAAT is fat located deeper in the body inside of the abdominal muscle layer and surrounds the organs within the abdominal cavity. It is believed that IAAT has a higher correlation to disease because it is more metabolically active^{16,17}.

Also, IAAT deposit's proximity to the hepatic portal vein, as well as the other organs, are other possible reasons why it is much more predictive of obesity related diseases.

Unfortunately, the internal IAAT deposit is much harder to measure than TAT or SAT. Traditional measures such as BMI and waist-to-hip ratios are not able to accurately estimate IAAT and thus cannot be used reliably to predict disease, especially within a research setting. Thus, in vivo imaging is required and the most accurate methods for quantification of fat in vivo are MRI and CT¹⁸. This is one of the key areas of research in obesity: determining the relationship between IAAT and disease progression and how we can use this information to prevent or treat these prominent and deadly diseases.

1.1.2 Current tests for fat distribution and disease

BMI is the most common measure of obesity in the world, due to its simplicity and low cost. All that is needed to calculate BMI is the height and the weight of the patient; equipment required is simply a scale and a tape measure. The exact calculation is the patient's body weight (in kg) divided by their height (in meters) squared. BMI results range from less than 15 kg/m² as very severely underweight, and greater than 40 kg/m² as very severely overweight or Obese Class III, as shown in Table 1.1.

Table 1.1 BMI Classification

Category	BMI range – kg/m²
Very severely underweight	less than 15
Severely underweight	from 15.0 to 16.0
Underweight	from 16.0 to 18.5
Normal (healthy weight)	from 18.5 to 25
Overweight	from 25 to 30
Obese Class I (Moderately obese)	from 30 to 35
Obese Class II (Severely obese)	from 35 to 40
Obese Class III (Very severely obese)	over 40

The relevant classifications for this thesis start above 25 kg/m² in the Overweight classification and all of the three obese classes above 30 kg/m². These classifications represent the at risk population, with higher rates of health conditions such as

hypertension, dyslipidemia, DM, CVD, stroke, amongst many others¹⁹. It is important to note that these classifications are only recommended for use in statistical scenarios and not for individual classifications. This is due to one of the flaws of BMI: BMI overestimates adiposity on lean individuals, and underestimates adiposity on those with less lean tissue. In particular, BMI has been shown to have sensitivities of only 36% in males, and 49% in females in comparison to body fat percentage²⁰. These are incredibly low sensitivities and thus BMI is more suited for large statistical studies that it isn't feasible to use more direct measures of adiposity. For this reason, and because BMI is much less sensitive to disease prediction than IAAT quantification, BMI is not optimal for research.

Waist-to-hip ratio (WHR) is another method for measuring obesity and is as simple as BMI. This technique uses the ratio of the circumferences of the waist and the hip to estimate adiposity. In the elderly, WHR has been shown to be a better predictor of mortality than BMI²¹. While WHR is a better estimate of the distribution of fat in the body, it still is not an accurate enough tool for use in obesity research. There are drawbacks such as inexact methodology for where on the body the waist and hip measurements should be made. More importantly, WHR is not the best indicator of cardiovascular risk factors²².

The problem with BMI and WHR is that they can only determine whether or not a patient is at risk and do not provide a measure of degree of risk. Therefore the optimal method for obtaining information about these diseases and their interaction with fat accumulation must be done with techniques able to measure IAAT. For this reason, imaging techniques are at the forefront of obesity research.

Single slice extrapolation is a popular technique for quickly estimating the amount of IAAT²³⁻²⁵. This involves scanning a single axial slice within the L2-L5 vertebrae region. As seen in Figure 1.5, this region is around the navel and has the highest accumulation of IAAT making it the best location for estimating the total IAAT. The reason this technique was developed was to account for the need to keep breath-hold times low for patients in the MRI. Breath holding in MRI is required due to motion causing artefacts within

collected images. Scanning a single slice and extrapolating IAAT volumes requires much shorter scan times than scanning the entire abdominal volume. This results in either better images or less time required for breath holds. In addition, this method also reduces the time needed for post-processing of the images as analysis only requires the segmentation of a single slice rather than a whole 3-dimensional set which can be approximately 80 slices. However, single-slice sampling fails when attempting to predict large variations in individual internal fat content²⁶, and when attempting to measure weight loss²⁷. Both of these are extremely important for research into obesity and its attributed diseases, as using techniques for weight loss or looking at individual variation and comparing it to disease is what is needed. Thus, multislice imaging is required for accurate measurement of IAAT in MR images²⁸.

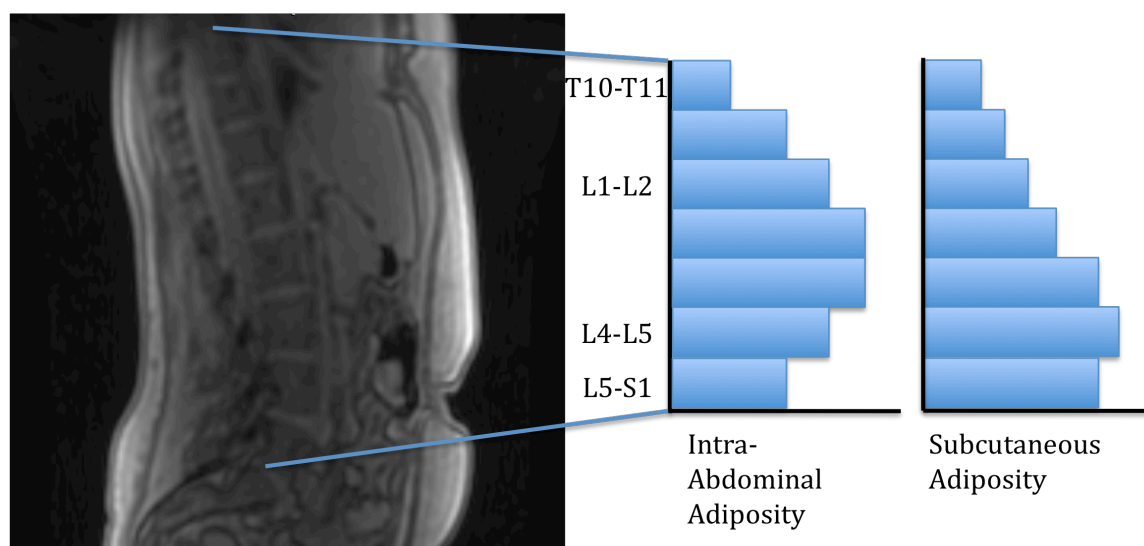


Figure 1.5 Adiposity in Spinal Regions

Depiction of the localization of adiposity in relation to position along the spine.

Intra-abdominal adiposity peaks between the L1 and L5 vertebrate, whereas subcutaneous adiposity peaks further down the spine²³. This distribution results in the associated apple-like shape for patients with higher IAAT, and pear-like shapes for patients with higher SAT.

A recent development is an automated technique to deal with the large post processing time of manual segmentation, called AdipoQuant²⁹. This method is available for human

MRI using water-fat images. It has been validated for use on lean and obese adults as well as lean and obese children. The average volume difference between full abdominal segmentations for this method was $(39.8 \pm 28.44) \text{ cm}^3$ ($1.1 \pm 0.7\%$) for SAT, and $(93.1 \pm 80.9) \text{ cm}^3$ ($5.0 \pm 3.3\%$) for IAAT. The method was also used with multiple water-fat imaging techniques (IDEAL³⁰, multipoint Dixon³¹) collected at different research laboratories. Most importantly this technique saves time, requiring only 2 seconds per slice in comparison to 8 minutes per slice with manual segmentation. The flexibility of this technique and insensitivity to the size difference between adults and children makes it a prime candidate for application to smaller test subjects.

There are many other techniques for the automated segmentation of adipose compartments in humans, and additionally there are many semi-automated techniques available. Another leading MRI technique uses a segmental shape model³² to identify the abdominal muscle layer and then perform segmentation. Other automated segmentation techniques that use histogram thresholding^{33,34} are available.

1.1.3 Rodent Research

While human research is important to advance our knowledge, rodent research can unlock information that would not be accessible from human research. This is due to the many techniques that are available for use on rodents, such as drug testing or invasive procedures. Research into the effects of chemical compounds on weight (loss or gain) would not be possible without preclinical testing on animal models. Rodent models are preferred due to their relatively cheap costs, and mouse models are specifically relevant as they are validated models of human obesity³⁵. Specifically, for obesity research, rodent models are much easier to regulate in terms of diets and monitoring the weight gain and loss over time. It is much more difficult to ensure strict following of controlled diets and ensure patients return at regular intervals for testing. In addition, studies that induce weight gain would not be recommended for use in humans, especially to the point of obesity. In essence, using rodent models such as the mouse allow cheaper, faster, and better regulated observation of the effects of obesity with less barriers to research than in humans³⁶.

1.2 MR Physics

1.2.1 Nuclear Magnetic Resonance and MRI Basics

Atomic nuclei with magnetic moments can be used to generate a signal. These magnetic moments appear in species that have odd numbers of protons, neutrons, or both. The most prominently used nucleus in MRI is hydrogen (^1H). This is due to its large natural abundance in the body in comparison to other nuclei. It is the most prevalent nucleus in the human body due to both lean tissue containing large amounts of water molecules, and fatty tissue containing molecules composed of many ^1H . The body is composed of 63% ^1H , and the next highest composition of MRI-studied nuclei is oxygen composing 26% of the human body³⁷. Not only is the high composition of ^1H important, but also it has a high natural abundance of a single isotope. 99.985% of hydrogen nuclei exist naturally as the ^1H isotope³⁸, making it a prime subject for use as more nuclei result in more signal. The high concentration of ^1H in the body allows it to be easily measured in comparison to other nuclei.

A combination of magnetic fields is used to manipulate the nuclei into producing a measurable signal in the MRI. The main magnetic field, or B_0 , is a constant magnetic field. When nuclei are placed within this field, the lowest energy state will be aligned with the direction of this magnetic field. There will still be a small component of the nuclei's polarity that is not aligned with B_0 in the higher energy state anti-parallel to B_0 . Figure 1.6 illustrates these alignments.

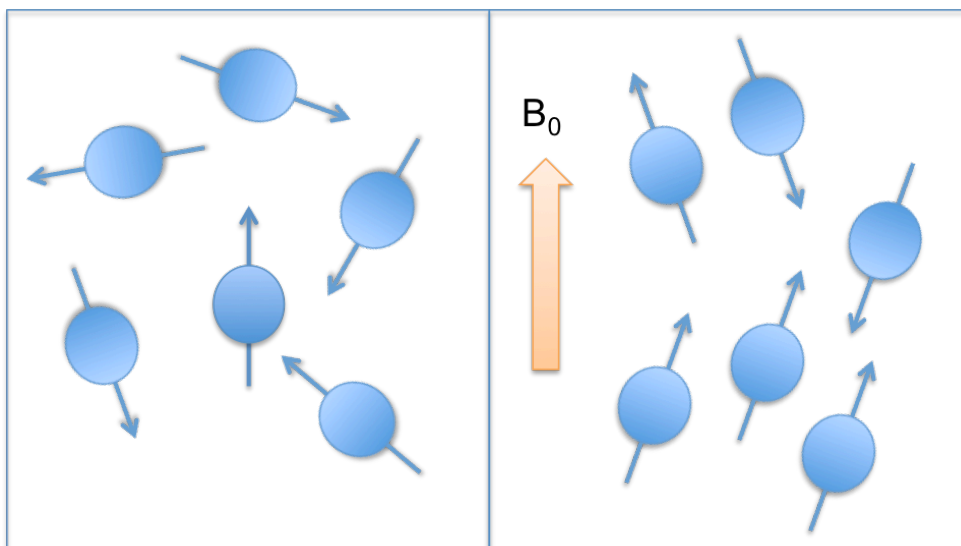


Figure 1.6 Effect of Magnetic Field on Magnetic Moments of Nuclei

Cartoon depiction of the direction of nuclei magnetic moments when placed within a magnetic field. Nuclei within the magnetic field have two energy states: a low-energy alignment parallel to the magnetic field, and a high-energy alignment anti-parallel to the magnetic field. Due to the energy differences between these states, the nuclei tend to align parallel to the magnetic field.

This magnetic field causes the nuclei to precess. The rate of precession that these nuclei experience is based on the strength of B_0 and a property of the nuclei called the gyromagnetic ratio (γ)³⁹. This property depends on the nuclei's atomic weight as well as its structure. Equation 1.1 models the precession of nuclei.

Equation 1.1

$$\omega_0 = \gamma B_0$$

Here ω_0 represents the angular velocity of the nuclear precession within the magnetic field. For ^1H , this velocity is $267.52 \cdot 10^6 \text{ rad/s}\cdot\text{T}$ or 42.577 MHz/T . With the

strength of B_0 at 3 T, ^1H precess at 127.6 MHz, which is within the Radio Frequency (RF) range.

1.2.2 Net Magnetization within a Magnetic Field

The alignment to the external magnetic field, B_0 , is governed by the tendency for the proton spins to align with the magnetic field and their ability to gain energy from thermal contact⁴⁰. This is according to Boltzmann probability theory where the number of aligned protons ($N_{||}$) depends on the total number of protons (N), Planck's constant (\hbar), the Larmor frequency of the protons (ω_0), Boltzmann's constant (k), and the temperature (T) as seen in Equation 1.2.

Equation 1.2

$$N_{||} \cong N \left(\frac{\hbar \omega_0}{2kT} \right)$$

The aligned protons can be manipulated by RF magnetic fields as a group, and thus we can concern ourselves with the response of the net magnetization of the nuclei rather than the individual responses. Figure 1.7 illustrates net magnetization. As our signal will depend on the number of protons within this group, the resulting MRI signal depends on the strength of the magnetic field and the temperature of the object. In the case of humans and animals, the temperatures are relatively consistent; meaning the largest factors contributing to the signal are the magnetic field of the MRI and the number of protons within the object.

In order to measure the signal from the nuclei we apply an additional magnetic field to force the nuclei out of equilibrium and tip the net magnetization. This additional magnetic field is typically a short pulse of milliTesla (mT) magnetic strength, and we denote this RF field as B_1 . As the precession is constant, the tipping process can be simplified by using a rotating frame with an angular velocity of the Larmor frequency. Therefore, the tip of the net magnetization (θ) will depend on the strength of the field (B_1), the gyromagnetic ratio (γ), and the amount of time the RF pulse is applied (τ)⁴¹. This relationship is displayed in Equation 1.3.

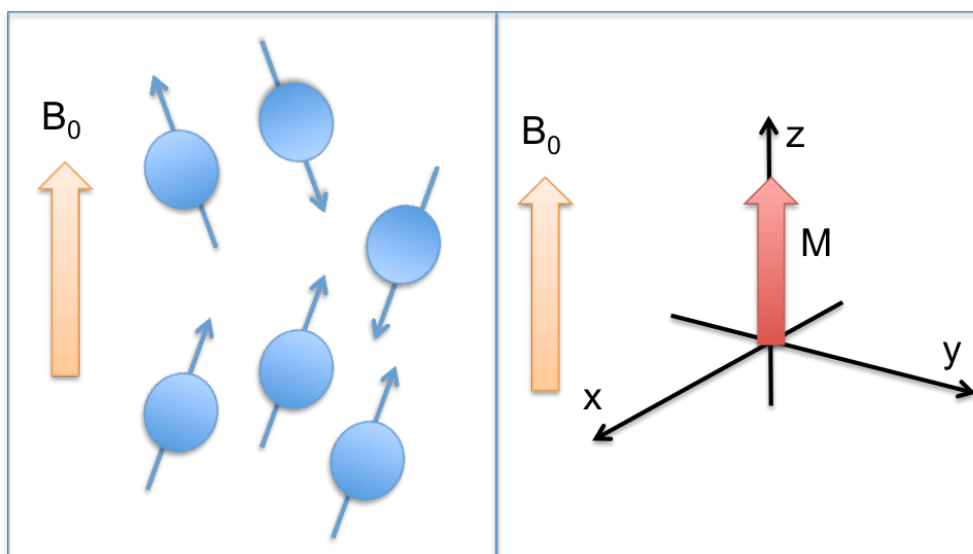


Figure 1.7 Net Magnetization of Nuclei in a Magnetic Field

Cartoon depiction of the summation of the direction of magnetic moments of nuclei within a magnetic field. As they tend to align with the magnetic field, net magnetization will be parallel to the magnetic field. These groups of nuclei experiencing the same magnetic fields are called “Spin Packets” and result in ease of calculations through use of net magnetization rather than individual magnetic moments.

Equation 1.3

$$\theta = \gamma B_1 \tau$$

After the time τ has elapsed the RF magnetic field is turned off and the nuclei precess back to the equilibrium magnetization. This return to equilibrium results in a varying magnetic field arising from the nuclei, and if there are nearby conductive materials, a current will be induced in them. A current will be induced in detector coils surrounding the nuclei that allow measurement of signal. The return back to equilibrium magnetization is governed by many properties including the tissue that the bulk of the nuclei are located in, such as fat or water.

1.2.3 Magnetization Relaxation

When the nuclei are placed in this magnetic field, they approach an equilibrium magnetization (M_0) dependent on absolute temperature and the external magnetic field B_0 ⁴². As the bulk nuclei are tipped out of equilibrium by the RF pulse, the net magnetization will return to equilibrium based on two relaxation properties. The first property is called spin-lattice relaxation, or T1 relaxation. After being tipped away from equilibrium, the net magnetization (M_z) will grow back towards equilibrium according to Equation 1.4.

Equation 1.4

$$M_z = M_0(1 - e^{-t/T1})$$

Thus the current longitudinal magnetization will exponentially grow back towards equilibrium over time (t) with a rate factor ($T1$) known as the spin-lattice relaxation time. The T1 is the time it takes for ~63% ($1/e$) of the magnetization to return to equilibrium after it has been perturbed by the RF magnetic field. Spin-lattice relaxation, or T1 relaxation, is based on the composition of the object including the mobility of nuclei. In addition, T1 relaxation rates will be greatly affected by magnetic field strength. Mobility of the nuclei is how easily they can rotate and vibrate within the object, resulting in energy transfers from the nuclei to the lattice surrounding them. Objects with more nuclear mobility (for example water, in comparison to fat tissues) will return to the equilibrium state slower, thus in most cases the T1 of more mobile objects are longer. For example, T1 times are 250 ms for fatty tissues and are 900 ms for water-based muscle tissues⁴².

Equation 1.5

$$M_{xy} = M_{xy}(0)e^{-t/T2}$$

The second relaxation property is called spin-spin relaxation, or T2 relaxation. This is the rate at which the net magnetization in the transverse plane decays back to zero, and is heavily dependent on neighbouring spinning nuclei. Equation 1.5 governs this rate of

relaxation. Here $M_{xy}(0)$ is the initial magnetization in the transverse plane, t is the time elapsed, and T_2 is the spin-spin relaxation constant. Spin-spin relaxation is typically much faster than spin-lattice relaxation, with the time constant being 60 ms for fat and 50 ms for muscle⁴². This relaxation occurs due to the dephasing or decoherence of transverse magnetization over time. Dephasing is the return to random orientation of the nuclear magnetization over time across the transverse axis and results in the net magnetization in the transverse plane being reduced to zero. This dephasing is shown in Figure 1.8.

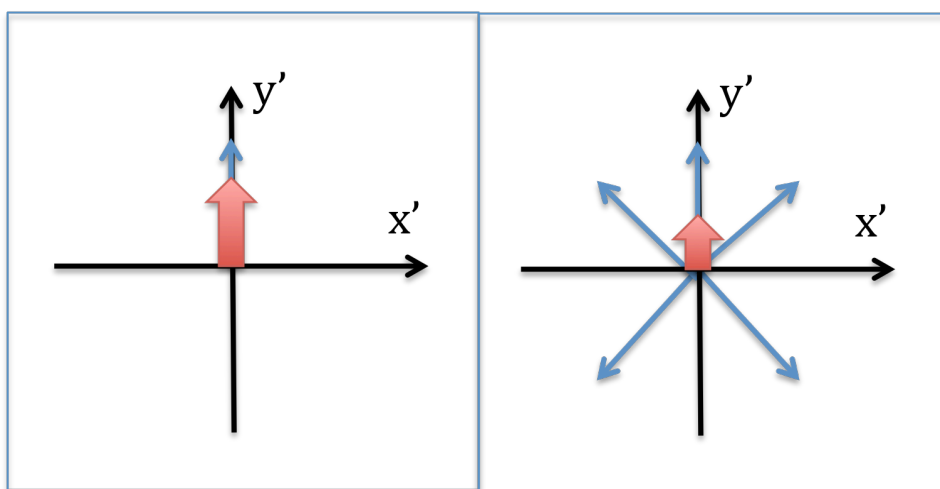


Figure 1.8 Dephasing of Transverse Magnetization

Cartoon depiction of decay of net magnetization in the transverse plane using a rotating frame of reference. The frame rotates at the Larmor frequency, resulting in the net magnetization appearing to remain in one direction. As the precession of nuclei move away from the Larmor frequency due to interactions between spins, the net magnetization decays to zero.

There is an additional effect on the relaxation of the transverse magnetization. As the decay rate is governed by the interactions of neighbouring spins, differences in the precession rates can cause this dephasing to happen quicker. A main source of this difference in precession is due to B_0 inhomogeneity. Unfortunately for our equipment we cannot create a perfectly equal field across the entire object, and this results in small differences in the magnetic field. These small differences will change the Larmor

frequency in that area, which in turn interferes with neighbouring nuclei causing a faster decay rate of transverse magnetization. This faster rate is called $T2^*$ and is described by Equation 1.6.

Equation 1.6

$$\frac{1}{T2^*} = \frac{1}{T2} + \frac{1}{T2'}$$

$T2'$ is the dephasing due to the magnetic field inhomogeneities that includes chemical differences, inhomogeneities in the main magnetic field, and any other sources causing non-ideal relaxation for the object's nuclei. Loss of transverse magnetization due to $T2'$ is recoverable as it is static and related to the magnetic field inhomogeneities⁴².

The spin echo sequence takes advantage of the dephasing of the transverse magnetization to produce an echo by using a 180-degree flip of the net magnetization. If we call the total time of this process TE (or echo time), the 180-degree flip would be applied at $TE/2$ to invert the phase the spins have acquired⁴³. As each of the nuclear magnetizations dephase at different rates, flipping them and allowing the phase to evolve over the same period of time will cause them to rejoin together. This causes a growth in transverse magnetization until it reaches a maximum at TE , which is called the echo. The next step is to localize the nuclei precession with small variations in the magnetic field, using gradient coils.

1.2.4 Resolution and Gradients

Varying the magnetic field across a direction will allow localization of the received signal. Localization requires the use of multiple directional gradient fields that are mT/m in strength. These gradients cause the Larmor frequency of the spins to be linearly proportional to their position⁴⁴, resulting in changes of 10 – 100 kHz across a human body at 3T. These differences in frequency of precession can be modeled using Equation 1.7.

Equation 1.7

$$\omega(r) = \gamma(B_0 + G(r))$$

Here r can be replaced with either x , y , or z . The gradient function ($G(r)$) is normally a linear function of the position. The z gradient or slice-select gradient is applied during the initial radiofrequency pulse. This gradient, in combination with the RF pulse's Bandwidth (BW), selects the region to be imaged. This gradient can either be used to select a volume to scan or it can be used to encode areas in the z direction to allow the volume scanned to be localized into multiple slices.

The next gradient used is the phase encoding gradient. This gradient encodes across the object in the y direction by adjusting the longitudinal magnetic field. This causes slight phase differences across the y direction that can be accounted for localizing the signal responses. To further localize, a final x gradient or frequency encoding gradient is applied to give us differences in the precession frequencies across the x direction of the object. This is when we acquire the signal that the nuclei produce. We now have localized signal for the x , y , and z directions of our object allowing us to fully reconstruct where the signal comes from in our object.

As a note, the frequency encoding gradients are repeated for each phase encode that we need to collect, and furthermore both of these are repeated for each slice select or z gradient that is needed. This causes the length of time required for our acquisitions to mainly depend on the number of slices and phase encodes required⁴⁵, while there is little dependence on the frequency encoding. The resulting signal acquired is the current induced by all of the precessing nuclei in the sample, within the area excited by the RF pulse. This results in a matrix consisting of phase on the y axis and frequency on the x axis. This matrix is known as 'k-space' and is the Fourier transform of the MR image, meaning the amount of phase and frequency encodes we use to map out our signal directly determines the resolution of our final image. Figure 1.9 shows an example of k-space and the Fourier transform image space.

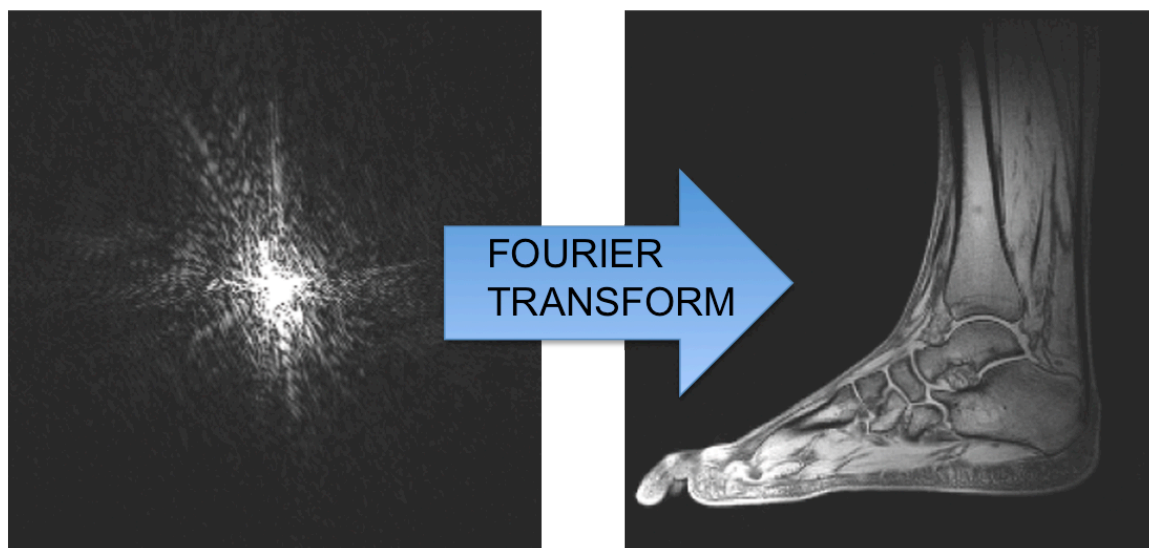


Figure 1.9 K-space and Image Space

(Left) K-space image, (right) reconstructed image. The k-space matrix is frequency vs. phase, resulting in the center of k-space containing low frequency, low phase information. The center of k-space contains low-resolution information about the image. The further out in k-space that the information is contained, the higher the resolution. To convert k-space information into an image, the Fourier transform is used.

Resolution determines the amount of detail visible in the image by the number of voxels in the image. This is a very important part of segmentation due to partial volume effects (PVE). PVE occur when a single voxel contains signal from two separate objects. In the case of segmentation, when fat tissue and water tissue are contained in the same voxel it can cause problems with segmentations. In most cases, the voxel size should be smaller than the size of the object. Unfortunately this is not always possible to achieve this with reasonable scanning parameters.

The resolution of the acquired images is dependent on how many phase and frequency encodes we acquire. To increase the amount of resolution there are tradeoffs that must be made. Keeping all other parameters the same, an increase in resolution will either increase the time of the scan or reduce the Signal to Noise Ratio (SNR)⁴⁵. SNR is needed to be able to identify where in the image the useful data is, and to separate that from the

background noise. To regain some of this SNR, the scans can be repeated and averaged and follows the relationship in Equation 1.8. Averaging noise will cause it to cancel out or lower intensity, whereas averaging the signal from the scanned object will increase the intensity in comparison to that noise. Unfortunately this greatly increases the scan times because each average requires a complete repeat of the scanning sequence. Thus we have a three-way tradeoff between SNR, resolution, and scan time.

Equation 1.8

$$SNR \propto \sqrt{N_{averages}}$$

1.2.5 Water-Fat Imaging

1.2.5.1 Chemical Shift

There are many MR acquisition techniques for analysis of fat content and water content. Most of these take advantage of the differences between the molecular composition of water and fat. In water molecules, the ^1H are bound to oxygen that pulls their electrons towards it, and there are relatively few electrons around the nucleus. This leaves the ^1H nuclei of water more susceptible to the magnetic fields than the ^1H in fat molecules. In fat molecules, the ^1H nuclei are typically bound to carbon atoms instead of oxygen. In this case, the electrons surrounding the ^1H are not drawn towards the carbon as much as they are to oxygen but instead remain associated with the ^1H . From this, a shielding effect occurs such that the ^1H experiences a smaller magnetic field than it would if it were in a water molecule. This results in measurable changes to the Larmor frequency based on a nuclei's local environment⁴³. This phenomenon is called “chemical shift” and has been exploited for analysis of fat content or removal of fat from the image. From the main fat peak to the water peak, the shift due to chemical composition is 3.5 ppm, as shown in Figure 1.10. Looking back at Equation 1.1, any change in magnetic field will cause a change in the frequency of precession. Therefore chemical shift results in the ^1H in fat molecules precessing at a slower rate than those in water molecules.

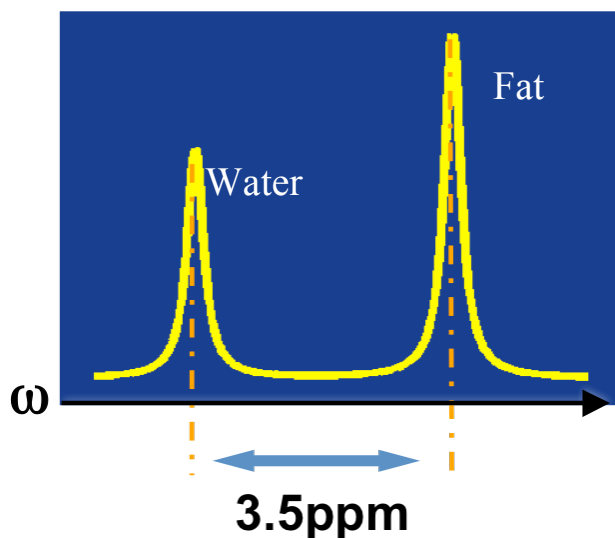


Figure 1.10 Chemical Shift between Water and Fat

Representation of the spectral difference between ^1H contained in water molecules and fat molecules. The precession of the nuclei in fat is slower than those in water due to the reduced magnetic field that they experience. This results in a difference of 3.5 ppm between the two peaks, or 428 Hz within a 3 T magnetic field.

1.2.6 Water and Fat Imaging Techniques

One early acquisition technique was called Fat Saturation. This involved an additional RF pulse prior to the initial RF pulse called a saturation pulse. This pulse is centered on the frequency where the fat precession would be, with a small bandwidth so that it does not affect the water molecules. This saturation pulse would be 180 degrees in order to completely flip the net magnetization of the fat nuclei (to $-M_0$). As the magnetization slowly grows back to equilibrium, the RF pulse covering both water and fat is then timed to when the fat magnetization reaches zero. This leaves the water magnetization in the transverse plane, and the fat magnetization untouched by this RF pulse. The disadvantage of this technique is that it requires the perfect bandwidth for the saturation pulse. In addition, there is not one singular fat peak but many due to the multiple species present in the body.

Another technique was developed to take advantage of the different precession rates of fat and water hydrogen nuclei. The theory behind the Two Point Dixon technique⁴⁶ is that if an image is collected when the fat and water are the same phase, and then another is taken when they are opposing phases, a simple addition or subtraction of the resulting images will return a water only or fat only image. The images collected are the In Phase (IP) image for when the water phase and fat phase are parallel, and the Out of Phase (OP) image for when the phases are anti-parallel. Problems arose using this technique mainly due to inhomogeneity in the main magnetic field. This inhomogeneity causes the IP and OP images to have a phase shift as shown in Figure 1.11.

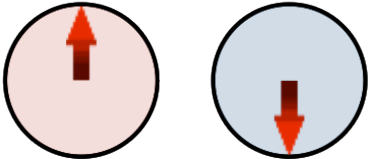
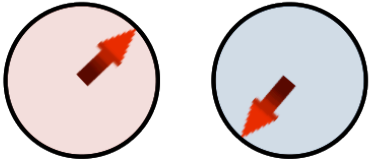
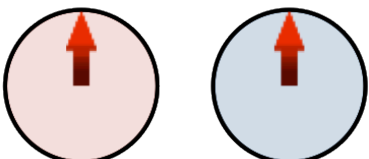
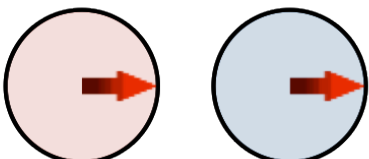
	No Field Inhomogeneity	B_0 Field Inhomogeneity
Phases in OP Image		
Phases in IP Image		

Figure 1.11 Effect of Field Inhomogeneity on Phases of Water and Fat

Representation of the relative phases of the water signal (red circle) and fat signal (blue circle) within the two images collected with Two Point Dixon. In a scenario with the correct B_0 , the IP and OP images add or subtract to give water-only and fat-only images. Due to slight variations in the B_0 across the image, different areas will experience different precession of nuclei. When the timing of image collection is based on the theoretical B_0 , areas with a shift in this B_0 will experience phase differences resulting in bias in both the fat and water images.

This inexact opposition results in biases that vary across the image, dependent on the range of differences in the magnetic field. In addition, this technique also treats fat as a single peak that causes difficulty in true quantification of fatty tissues.

The next development in water-fat imaging was the Three Point Dixon technique^{47,48}. This technique was developed to account for the variation in the main magnetic field by estimating what the field would look like based on the collected images. Collecting an initial OP image, an IP image, and then a second OP image allows this estimation. By using the two OP images it is possible to determine the change in phase over time and allows determination of the magnetic field in that location. This can then be used to correct the IP image, and then fat and water images are created in the same method as the Two Point Dixon technique. This method was fairly robust but suffered in areas where water and fat content were almost equal. Figure 1.12 shows the Number of Signal Averages (NSA) in a 100% water voxel, and 50% water voxel.

NSA is a measure of how the technique performs based on the SNR. It is a measure of how many effective averages your final images has, and optimum NSA is equal to the number of images you collected. The optimum SNR for the Three Point Dixon method would be as if you averaged 3 images, or had an NSA of 3. In the 50% voxel, the Three Point Dixon gives an NSA of 0. This decrease to zero drops rapidly as the content of the voxel approaches 50%. This happens due to the lowered information from deconstructive interference when taking an OP image, as a 50% voxel will result complete deconstruction of signal due to the opposing fat and water in the voxel. From this we can conclude that to not lose data, we should avoid collecting OP images.

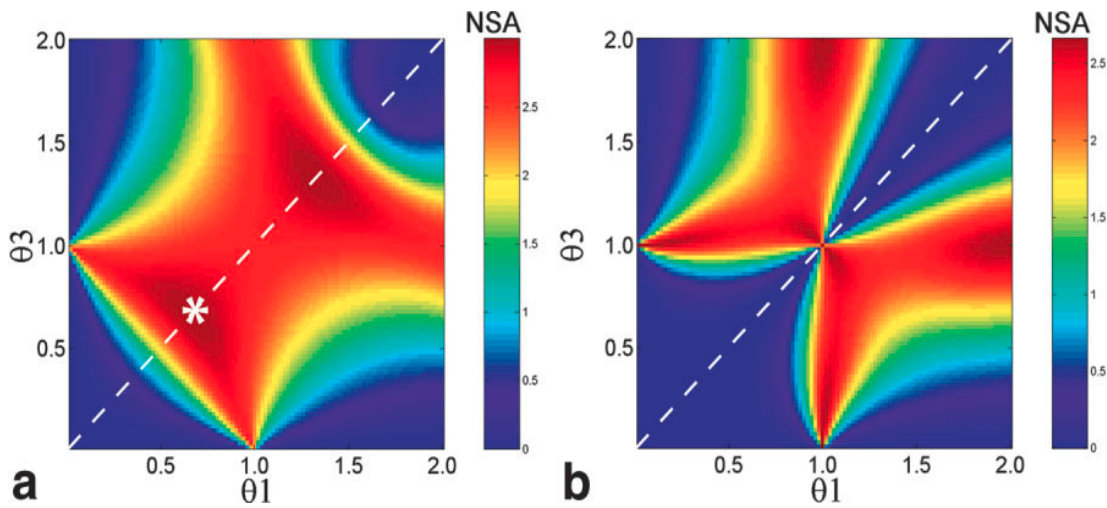


Figure 1.12 NSA for Three Point Dixon at Different Echo Times

Heat map of the NSA of a voxel containing 100% water (a) and 50% water (b). Axes are the angle separation of the fat signal between the first and second echo time (θ_1) and the angle separation between the second and third echo times (θ_3). The second echo time is centered on the alignment of the fat and water signals (in phase). The dashed white line covers angles with symmetric separation, a requirement for Three Point Dixon. An asterisk marks the optimum angle separation for Three Point Dixon. [Image from Reeder S *et al.* 2005⁴⁹]

This led to the development of the Iterative Decomposition of water and fat using Echo Asymmetry and Least-squares Estimation (IDEAL)⁴⁹. This technique involves using NSA maps to determine the optimal echo times to collect images for reconstruction of the fat and water images. While previous water-fat techniques used symmetric echoes to allow addition and subtraction as the simplest way to obtain the water and fat images, this technique used asymmetric separation of echoes. These echoes were optimized so that the angles of separation between the phase of water and fat signals were $\frac{-\pi}{6}, \frac{\pi}{2}, \frac{7\pi}{6}$. In this process the field map is iteratively determined after each images is collected according to the relationship in Equation 1.9.

Equation 1.9

$$S \propto \left(\rho_w + \rho_f e^{i \frac{\gamma}{2\pi} \Delta f \cdot TE} \right) e^{i \frac{\gamma}{2\pi} \Delta B_0 \cdot TE}$$

While this technique is the most robust of the previously described techniques, it still suffers from the same problem that Fat Saturation suffers from. Fat is made up of many species of molecules, all with different amounts of electrons shielding the proton nuclei. These different species have different chemical shifts, as shown in Figure 1.13. The different levels of shielding depends on the way the electrons are organized, which is dependent on what types of bonds are present between the Carbon atom and the rest of the molecule. This results in an inability to correctly quantify adipose tissue due to some fat species being present in both the water and the fat images. Fortunately, more information is available about these additional peaks, such as their relative position and height compared to the water peak. The summation can be added into the relationship in Equation 1.10 to enhance our image results.

Equation 1.10

$$S \propto \rho_w + \rho_f \sum a_n e^{i \frac{\gamma}{2\pi} \Delta f_n TE}$$

Finally, there is one additional factor that needs to be accounted for to better quantify fat in these images. The additional relaxation of nuclei due to inhomogeneities in the magnetic field cause bias in the final images if not taken into account⁵⁰. Therefore, we need at least one additional image to solve for R2* (inverse T2*) and adapt our variables as shown in Equation 1.11.

Equation 1.11

$$S \propto \left(\left(\rho_w + \rho_f \sum a_n e^{i \frac{\gamma}{2\pi} \Delta f_n TE} \right) e^{i \hat{\psi} \cdot TE} \right)$$

$$\hat{\psi} = \frac{\gamma}{2\pi} \Delta B_0 + \frac{i}{T2^*}$$

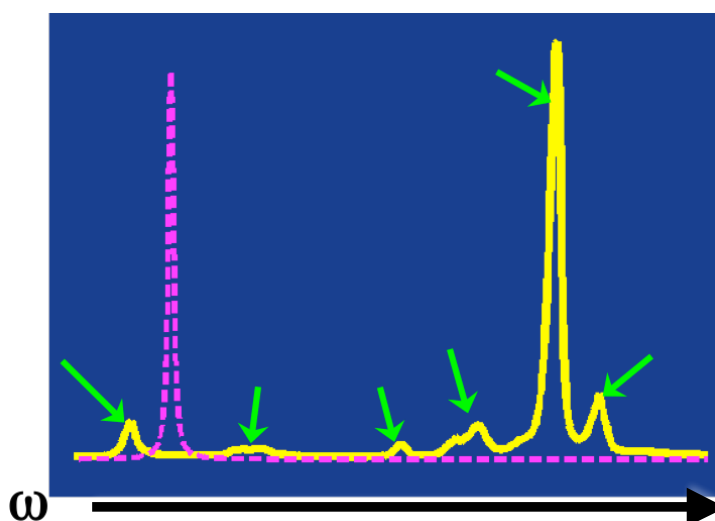


Figure 1.13 Spectrum of ^1H in different Fat Species

Relevant spectrum for ^1H in fat molecules. Green arrows mark the different chemical components of fat, and the purple dashed line represents the spectrum from ^1H in water. The separation and relative heights of the fat peaks will stay consistent and can be accounted for.

This is currently the preferred technique for quantification of fat. As this method uses an iterative process of fitting the image results to the theoretical values, the best results can be achieved by maximizing the number of images taken. As it is simply not feasible to acquire endless images, the currently accepted number of images taken for $R2^*$ Corrected IDEAL is six as this provides the best balance between acquisition time and accuracy of the fit.

1.3 Fat Segmentation

Several automated techniques for segmentation of fat have been proposed, and most of them rely on the muscle layer between the IAAT and SAT. As this layer is lean muscle it is bright on water images and darker than the fat in T1 images. This difference in signal intensity makes it theoretically possible for identification using automated segmentation based on simple thresholds.

1.3.1 Mouse Anatomy

In rodents, the same muscle layer is present separating the entire subcutaneous adipose deposit from the intra-abdominal adipose deposit. However, difficulties arise from using the muscle layer for automated segmentation because there are differences in the muscle layer between humans and rodents. The primary difference is the size of the muscle layer. Recent studies have shown the layer to require a resolution of 80 μm in lean mice, and as small as 50 μm for obese mice⁵¹. This means that any image resolution larger than this will cause PVE over this layer. Another area of difficulty is that high-resolution images obtained from rodents have shown that this muscle layer doesn't fully separate the IAAT from the SAT⁵². This is especially problematic for region growing techniques, as there is not a full barrier separating the two sections.

There are additional differences between human and mouse images that must be addressed. The position of the hips and legs in mice is problematic for segmentation techniques due to their proximity to the muscle layer. In humans, the water signal from the legs is far enough removed from the abdomen to ignore in segmentation of the muscle layer. In mice, ignoring the leg muscles causes inclusion of fatty tissues in the legs or misclassification of subcutaneous fat located near the edges of the legs. A more difficult problem to deal with is the superficial fascia – a small layer of lean tissue within the subcutaneous adipose tissue shown in Figure 1.14. This layer is difficult to account for due to its small size and inconsistent presence in MR images. Due to its small size, typically the superficial fascia does not affect the automated segmentation, but in some locations in the mouse it is thick enough to cause the automated segmentation to fail. Specifically within regions near the lungs, the fascia has a low enough fat content and large enough size to be readily apparent. In humans this is not as problematic due to the size difference of the fascia compared to the abdominal muscle layer, but in mice the fascia is approximately the same size as the abdominal muscles layer near the lungs. Extra steps are required to ensure that the fascia is not mistaken for the abdominal muscle wall. In addition, the fascia inconsistently appears in some abdominal images close to the mouse hips. These two differences in the mouse anatomy should be accounted for or at least understood when developing segmentation techniques for mice.

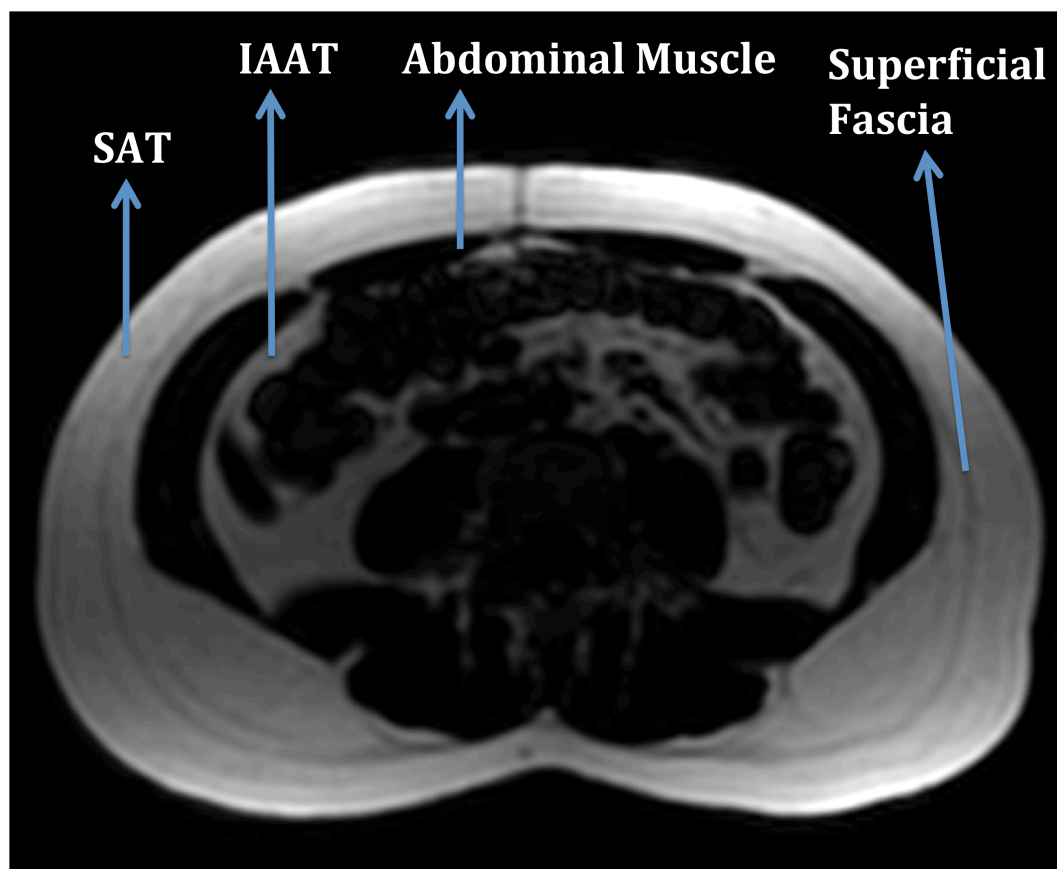


Figure 1.14 Superficial Fascia in a Human MR Image

Fat only axial image of a human. The SAT is separated around the body by a thin layer with less fat content known as the superficial fascia. As seen in this image, the size and intensity of the fascia greatly differs from the size and intensity of the abdominal muscles surrounding the IAAT. Thus in human automated segmentation the fascia can largely be ignored when trying to locate the abdominal muscle layer.

1.3.2 Rodent segmentation techniques

The primary method for quantification of adipose tissue in rodents is currently manual segmentation. Manual segmentation of T1 weighted images has been validated vs. weighing the tissues⁵³ proving its worth as a non-invasive technique for measuring internal fat. Furthermore, IDEAL imaging has been shown to be a more accurate method for manual segmentation than T1 images because T1 images having the same signal intensity values in liver tissue and adipose tissue. In addition, some organs, such as the

bowels, are easily mistaken for adipose tissue in T1 images⁵⁴. This leaves manual segmentation of IDEAL images as the optimal route for quantification of adipose tissue.

The base methods for manual segmentation require a threshold or connected threshold growing technique. The threshold is performed on Fat Only Images to create a total adipose image. This image is still prone to intensity variation but does not include organs such as the bowels, in comparison to T1 weighted images. This threshold is slice specific and is based on the operator's subjective judgment of an appropriate threshold. From the total adipose image, the subcutaneous adipose tissue is removed to create an IAAT image. Then the SAT image is created by a simple subtraction of the IAAT from the TAT.

A recent development, and the first fully automated MRI segmentation technique on a mouse model, uses a region growing technique⁵². For this method, the authors used a 9.4 T MRI, T1 weighted images, and maximized their resolution at approximately 0.2 mm to attempt to fully resolve the muscle layer boundaries. As they could not fully resolve the muscle layer even at this resolution, they chose to adapt the region growing to account for the small connections between the IAAT and SAT. This technique begins by automatically selecting locations acceptable for seeding the region growing, and then trims these based on several limitations. After reducing the possible seeding locations, competitive region growing is started between the IAAT and SAT where the algorithm adds pixels in areas furthest from the edges first. In this way, the region growing fills up all of the internal tissues before going towards the edges of the IAAT where the SAT and IAAT compete in the small areas where the muscle layer doesn't separate the two deposits. Bland-Altman analysis comparing to manual segmentation resulted in a mean difference of $(0.85 \pm 0.8) \text{ cm}^3$ for the TAT and $(1.0 \pm 1.3) \text{ cm}^3$ for IAAT.

Another recent technique for automated segmentation in mice uses a segmental shape model⁵⁵ to identify the abdominal muscle layer and separate the deposits. This method acquired T1 weighted images on a 7.05 T MRI. Segmentation procedure involved identifying the body contour, and then shrinking the contour until it reached the abdominal muscle layer. After this, a shape constraint was enforced to revise the

abdominal muscle contour based on distance from the body contour. To account for odd shapes in the body contour, this technique employed a segmental weight template to determine where variance in the body contour's shape was more likely to occur, and that the dorsal and ventral areas typically have a similar shape. Finally, a distance constraint was added to keep the abdominal muscle contour from going too far into the abdominal cavity. Average Dice coefficients in comparison to manual segmentation were 0.941 for TAT, 0.935 for SAT, and 0.920 for VAT.

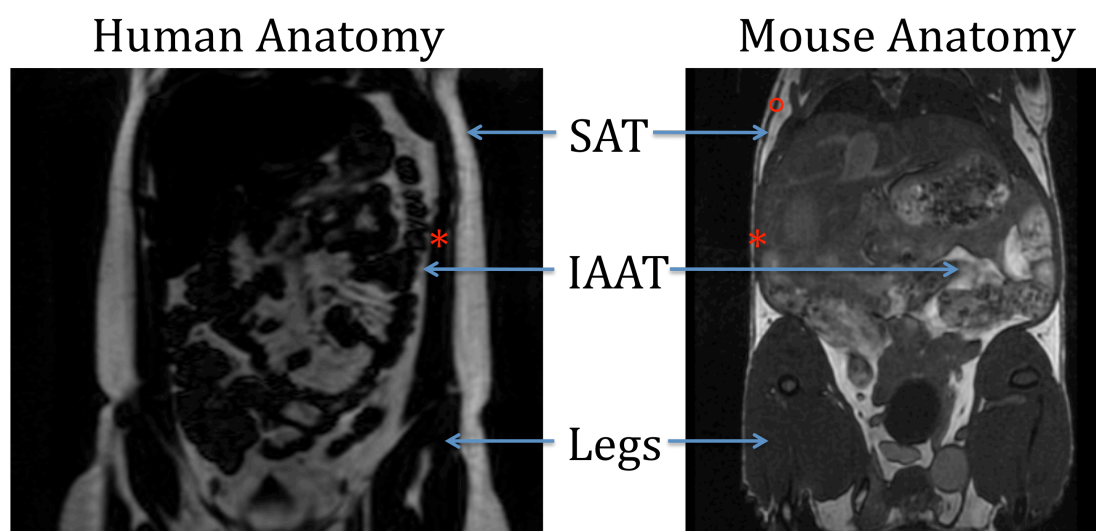


Figure 1.15 Differences in Anatomy

A comparison of a fat only image of a human abdomen (left) and a high resolution Balanced Steady-State Free Precession image of a mouse abdomen (right). Note the differences in abdomen shape and distribution of adiposity. The abdominal muscle wall is highlighted by a red asterisk in both images. The superficial fascia is highlighted by a red circle in the mouse image and is not visible in the human image. [Mouse Image Courtesy of Dr. Paula Foster's Lab]

1.3.3 Limitations of current techniques

The main limitation of manual segmentation is the time investment required to perform the analysis on large or multiple data sets. Manual segmentation typically requires approximately 8 minutes per slice, but can be much longer depending on the slice.

Longer times are required on slices with lower resolution, with objects of similar intensities to fat (such as a fatty liver or bowels), and with more ambiguous ranges of intensities. In situations such as these, the time requirement of manual segmentation is much higher due to the extra care required in selecting the proper threshold ranges and boundaries of the fat deposits.

In addition to the time required for manual segmentation of each slice, training time is an important consideration. Operators must understand how to use the segmentation tool, and must be familiar enough with the mouse anatomy on a fat only image to properly segment the appropriate tissues. This adds to the already large time costs of manual segmentation. Furthermore, even with training, inter-operator differences is a non-negligible problem with manual segmentation. This is especially important in studies involving weight gain or loss as smaller changes in adipose content could be within the error range of manual segmentation. To worsen this problem, intra-operator differences have also been established in manual segmentations, so using the same operator for every data set does not eliminate the problem of variation in the results.

While the region growing method is performed on high resolution images, the collected images suffer from more issues with signal variations in the T1 weighted images due to the use of 9.4 T MRI to collect the images. Higher MRI field strengths are associated with higher variations in the static field, resulting in large intensity differences across collected images. This will cause issues with adipose quantification as lower intensities will be removed from the image, or qualified as lower fat pixels when they are just areas of lower field strength. In essence, the flaws of not using a truly quantitative method of imaging water and fat results in a less accurate method for quantification with variation between scans causing non-negligible differences in adipose quantification.

The region growing method was developed to account for the small connections between IAAT and SAT so that no leakage of the regions would occur. However, in the final segmentation images it is readily apparent that there is still significant intrusion of the IAAT label into the SAT images, mainly at the posterior side of the mice. Finally, the inconsistency of labeling of tissues outside of the abdominal cavity causes issues in

comparing subjects, and possibly even comparing the same subject to itself. If the algorithm consistently labeled the region below the abdominal cavity as IAAT, it could be accounted for and wouldn't cause any issues. Unfortunately, its inconsistent labeling reduces the algorithm's reproducibility on different images.

There are similar limitations to the segmental shape technique. This technique also uses T1 weighted images for analysis, but adjusts intensities of images with the adaptive fuzzy C means segmentation. This clusters intensities within the body of the mouse into adipose, muscle, and organs. While this reduces some problems with loss of intensity, it does not eliminate the problem of misidentification of organs within the T1 ranges of adipose (bone marrow, bowels, liver). In addition, the segmental shape template and other constraints are all based solely on obese mice within their hardware setup. The variation in shape and position of the abdominal muscle layer and body contour is much less predictable when including lean mice and using a hardware setup that is not as constrictive on the mouse bodies.

1.3.4 Proposed Solutions / Thesis Objectives

The purpose of this thesis is to address the current challenges with automated rodent segmentation by creating a rapid, accurate, flexible technique that is easily transferred to human research. To do this, I propose an adaptation to the currently existing AdipoQuant algorithm with adjustments to account for the major differences between mouse images and human images. This allows use of fat fraction images for analysis and quantification over fat only images and T1 weighted images allowing a much greater accuracy in quantification. In addition, using a 3T MRI keeps the technique applicable to human research, as these MRI scanners are clinically available.

My hypothesis is that automation of the technique will allow more precision in the calculations and the reproducibility will be measured to ensure that small variations in adipose volumes can be quantified using this technique. Using fat fraction images should also reduce the amount of variability between images allowing further improvement in reproducibility.

These adaptations include solutions for the higher amount of PVE, the effect of the PVE on the muscle layer, the size of the muscle layer, the superficial fascia, and the leg position in mice. Thus this thesis describes the use of a 3 T MRI to collect IDEAL images of mice at relatively low resolution and validates the use of an adapted automatic segmentation technique.

2 Validation of Volumetric MRI Adipose Analysis on Mice Using a Fully Automated Segmentation Method

2.1 Introduction

Obesity is an increasingly costly disease associated with chronic diseases such as type II diabetes, cardiovascular disease, and cancer^{7,56}. Adipose tissue volume measurement is necessary for investigating effective treatment of obesity and its related diseases. Total Adipose Tissue (TAT) and Subcutaneous Adipose Tissue (SAT) can be estimated with techniques such as BMI, waist to hip ratio, and skin fold calipers. However, only Intra-Abdominal Adipose Tissue (IAAT) has a strong correlation to the occurrence of obesity related diseases^{16,17}. Magnetic Resonance Imaging (MRI) is suitable for measuring IAAT due to the inherent differences in image contrast between fat and other tissues.

MRI using T1-weighted image acquisition at 0.35 Tesla (T) has been shown to be a sensitive, reproducible, noninvasive, and safe method to determine the distribution of adipose tissue⁵³. Unfortunately, T1-weighted quantification of IAAT is confounded by other bright structures like blood vessels or bowel contents that may be mistaken for adipose tissue⁵⁷. Pulse sequences used to obtain water-fat separation give quantitative fat fraction images where each voxel (volume-pixel) provides a measure of the percentage fat. This makes it the optimal technique for determining quantitative volumes of fat non-invasively.

Once the images are acquired, segmentation of the compartments of fat is required for analysis. Manual segmentation is tedious and time consuming especially for large data sets. It is important to distinguish anatomy to avoid classifying other organs, such as the liver or bowels, as fatty tissue and this requires substantial training. To alleviate these problems, there are many automated segmentation algorithms for measuring the fat deposits^{32,33,34}. Automation allows rapid analysis that isn't prone to intra- and inter-

operator differences, leading to more precise and reproducible results. This is very important in longitudinal mouse models as small changes of fat may be missed if intra- or inter-operator differences are present. Furthermore, automation removes the training requirement for manual segmentation. It is important to distinguish anatomy to avoid classifying other organs, such as the liver or bowels, as fatty tissue.

Animal models are advantageous for obesity research because they allow careful control of disease models, have lower costs than human research, and allow research that would not be ethical on humans³⁶. This is particularly relevant for obesity research where animal models allow measurements to be made first on the normal weight animals and then disease progression can be monitored as fat is accumulated. Mouse models are well established for obesity in humans³⁵, but mice add additional difficulty to current automated segmentation methods due to their small size compared to humans. As a result, much higher resolution images are required for mice than humans; however, it is not currently possible to acquire images of mice with high enough resolution to have voxels of similar relative size (in relation to full body size) to human voxels. This means that mouse MRI has a relatively lower resolution compared to human MRI. In addition, there are minor differences in anatomy between mice and humans, such as positioning of limbs and incomplete separation of fat compartments. A layer of muscle separates the IAAT and SAT. In humans this layer is large and completely separates the two fat deposits, whereas in mice this layer is much thinner relative to the mouse size, and does not seem to fully separate the deposits even at high resolutions⁵². Another issue is the relative size of this muscle layer with the superficial fascia. This small layer in the subcutaneous adipose tissues appears to be relatively the same thickness as the muscle layer.

Here we propose a method to address the issues caused by relatively low-resolution mouse images. This method will be adapted from a currently existing human adipose quantification method²⁹ in order to apply it to a mouse model. This method will be tested with water-fat images collected from a 3T MRI with resolutions as low as 0.7 mm x 0.7 mm in the axial plane. This will allow other research to be performed simultaneously with the fat quantification as well as promote longitudinal research.

2.2 Methods

2.2.1 MRI Acquisition

Following approval by the institutional Animal Use Subcommittee, *in vivo* data was collected from 13 mice (C57BL/6J): 7 on a Western diet consisting of 40% of calories from fat, 6 on a normal chow diet. All animals were scanned with a custom-built ^1H RF coil in a GE 3.0 T MR750 (GE Healthcare, Waukesha, WI). Images were collected with an IDEAL [3] pulse sequence over 40 minutes (NEX = 13, six echoes, TE = [2.2, 3.2, 4.3, 5.3, 6.4, 7.4] ms, TR = 14.02 ms, FOV = 120 mm x 54 mm x 34 mm, Resolution = 0.8 mm x 0.7 mm x 0.7 mm, Flip Angle = 3°).

2.2.2 Automated Segmentation

The segmentation algorithm was adapted from a validated human MRI segmentation method called AdipoQuant²⁹. The first step identifies background noise to separate it from the mouse volume. To accomplish this, a k-means clustering algorithm was used on the total signal image (the sum of the signal from the water image and the fat image). This process is illustrated in Figure 2.1. The mouse method has increased number of classes to account for the lower SNR in mouse images compared to human images on a 3T MRI. The lower classes were discarded (noise, lungs, bone-filled regions), and the upper classes were kept (fat and water tissues) and converted into a binary tissue volume mask. Small holes in the mask were filled using a hole-filling algorithm.

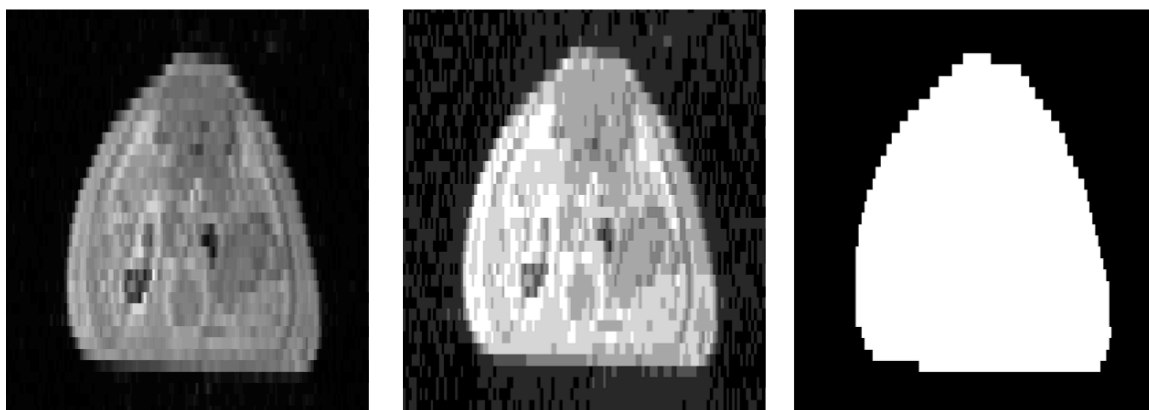


Figure 2.1 K-means on In Phase Image to Create an Image Mask

Axial images within the lower abdomen of an obese mouse. From left to right: in phase image, k-means image, and the resulting total tissue mask. Image intensities are binned into equally separated groups or classes by the k-means segmentation. The lowest classes in the k-means images are discarded as noise, and the higher classes are kept as tissue and then filled to create a mask. This mask is then used to remove noise from the fat fraction image.

The second step created a mask of the adipose tissue as outlined in Figure 2.2. The tissue volume mask was applied to the fat fraction image to remove noise and non-tissue compartments. A threshold of 70% was applied to the masked fat fraction to select high fat content areas. This fat mask was expanded to nearby voxels greater than 60% fat fraction. A much higher fat fraction than the human method is required here (the human method expands to voxels with 45% or higher fat fraction) due to the lower relative resolution and the very small muscle layer separating the two fat deposits. This lead to partial volumes on the muscle layer and the adipose tissue resulting in voxels with up to 65% fat fraction. As the muscle layer is usually only one voxel wide, the expansion of the fat selection consistently selected the muscle layer as fat if a lower fat fraction was used.



Figure 2.2 Adipose Tissue Mask Creation

Axial images within the lower abdomen of an obese mouse. From left to right: Fat only image, greater than 70% fat fraction voxels, total adipose tissue voxels. The voxels from the center image are used to locate the connected fat that sits between 60% and 70% fat fraction, creating the total adipose voxels. The center image shows that thresholds alone will not accurately find all of the adipose tissue.

Next the organs and muscles were located using a fat fraction less than 65% within the tissue volume mask. Unfortunately, this threshold cannot be used across the volume due to the superficial fascia as displayed in Figure 2.3. To account for the superficial fascia around the chest of the mouse, the threshold for water tissue around the diaphragm was reduced to fat fraction less than 40%. Less than 40% fat fraction cannot be used across the entire volume as high fat fraction voxels over the muscle layer would be removed, but this typically only occurs around large fat deposits closer to the pelvis. Thus, the fascia causes additional issues close to the pelvis and was accounted for by dilating a mask of the skin that was removed from the water tissue mask. The fascia did not cause issues between these two areas.

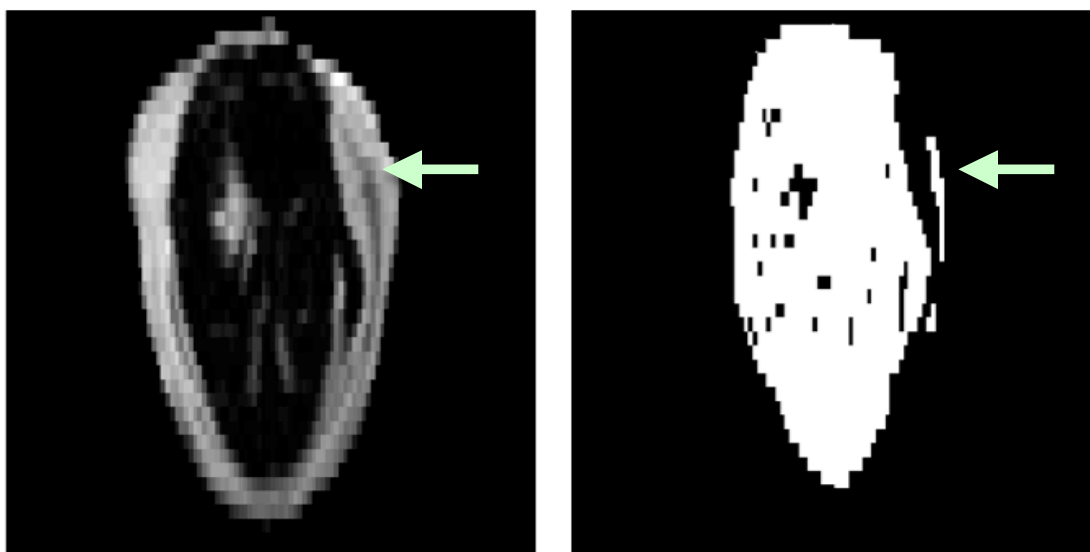


Figure 2.3 Superficial Fascia in a Mouse MR Image

Axial image of an obese mouse at the level of the heart and lungs. On the left is the fat only image, and on the right is a threshold of fat fraction less than 60%. As noted in Figure 1.14, the fascia surrounds the mouse body and is within the SAT.

However, the mouse fascia is much larger relative to the abdominal muscle layer, shown with the arrows. As they are closer in size, it is important to take into account the fat fraction of the fascia to avoid misclassification of the layer as part of the abdominal muscles.

The constructed organ and muscle mask was then converted into polar coordinates, as shown in Figure 2.4. The new matrix contained the outer edge of the organ and muscle mask (the muscle barrier between the IAAT and SAT) as the lowest pixel in each column. This is then smoothed within the slice to have a solid barrier at the edge of the muscle layer. Further smoothing is applied to ensure consistency between slices. Figure 2.5 shows the selected pixels for the slice and the final smoothed result. The strictness of the smoothing algorithm within the slice was increased in comparison to the human method to account for more missing pieces of the muscle layer due to PVE. However, smoothing was reduced between slices due to greater variation between slices.

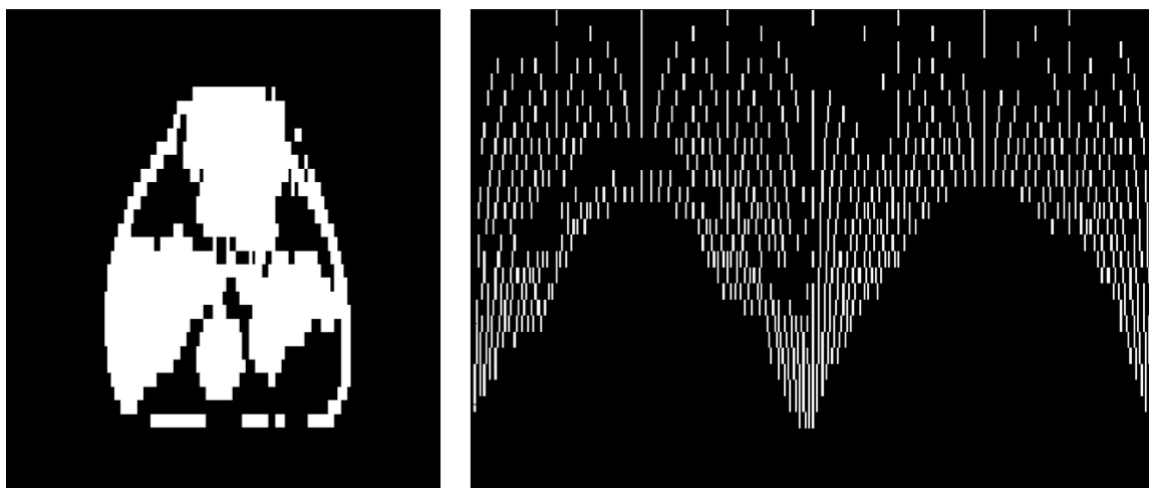


Figure 2.4 Water Mask and Polar Water Mask

Axial images within the lower abdomen of an obese mouse. The left image is a mask of fat fraction less than 65% (with noise removed), the right is the same image converted to polar coordinates. Conversion to polar coordinates is effectively an unwrapping of the image from the center. This means that voxels closer to the center of the Cartesian image will be at the top of the polar image. Each voxel further from the center in Cartesian is lower in polar coordinates.

This surface was then converted back into Cartesian coordinates and filled to complete a mask of the visceral cavity. The mask is then applied to the total adipose mask to separate the IAAT from the SAT. This can be seen in Figure 2.6.

Finally, summing the fat fractions in each slice and multiplying by a voxel to volume conversion factor allowed determination of the volumes of fat. The conversion factor was determined by the imaging parameters of the scans. The segmented volumes could then be viewed in 3D as separate rotatable images, shown in Figure 2.7. The full segmentation process is summarized in Figure 2.8.

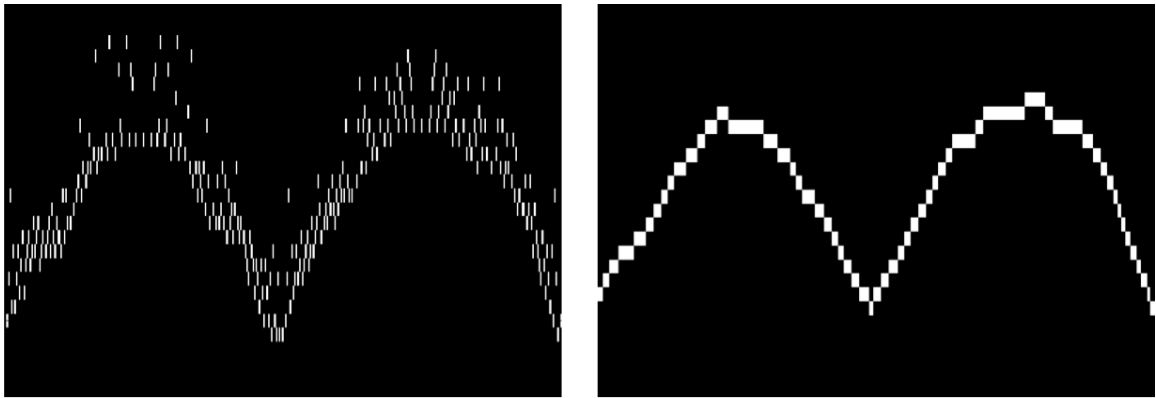


Figure 2.5 Lowest Voxels in Polar Coordinates and Smoothing

Axial images within of the lower abdomen of an obese mouse converted to polar coordinates. The left image shows the lowest voxels from the originally converted polar image shown in Figure 2.4, the right image is a smoothed, continuous line covering the bottommost voxels. The lowest voxels in the left image can be towards the center of the Cartesian image, but most are at the edge of the abdominal muscle layer. Note that voxels outside of this abdominal layer (fascia, artefacts) will cause misalignment.



Figure 2.6 Intra-Abdominal Cavity

Axial images within the lower abdomen of an obese mouse. From left to right: Total adipose image, intra-abdominal cavity, and total adipose image with abdominal cavity mask applied in green. The abdominal cavity is created by filling above the smoothed boundary in Figure 2.5, and converting back to Cartesian coordinates. This mask of the cavity is then applied to the total adipose image to separate the IAAT from the SAT.

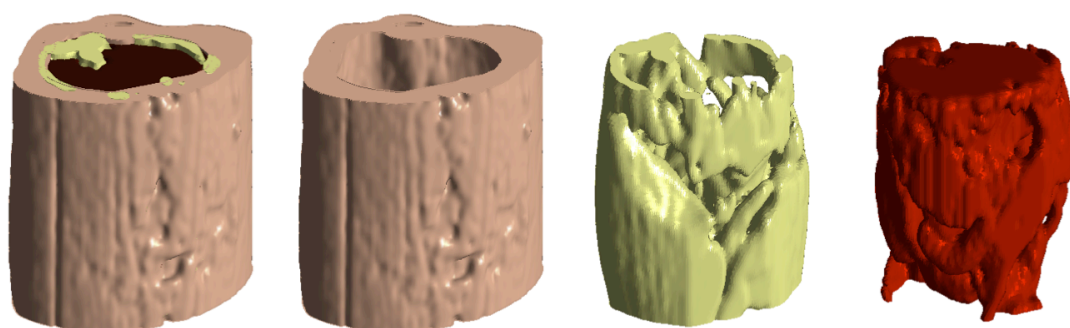


Figure 2.7 3D Segmented Volume Images

3D renders of a full obese mouse abdomen. From left to right: Total tissues image, SAT only, IAAT only, Water tissue only. Volumes range from the dome of the diaphragm to the base of the pelvis and are displayed with the diaphragm at the top and the ventral side of the mouse facing out of the page.

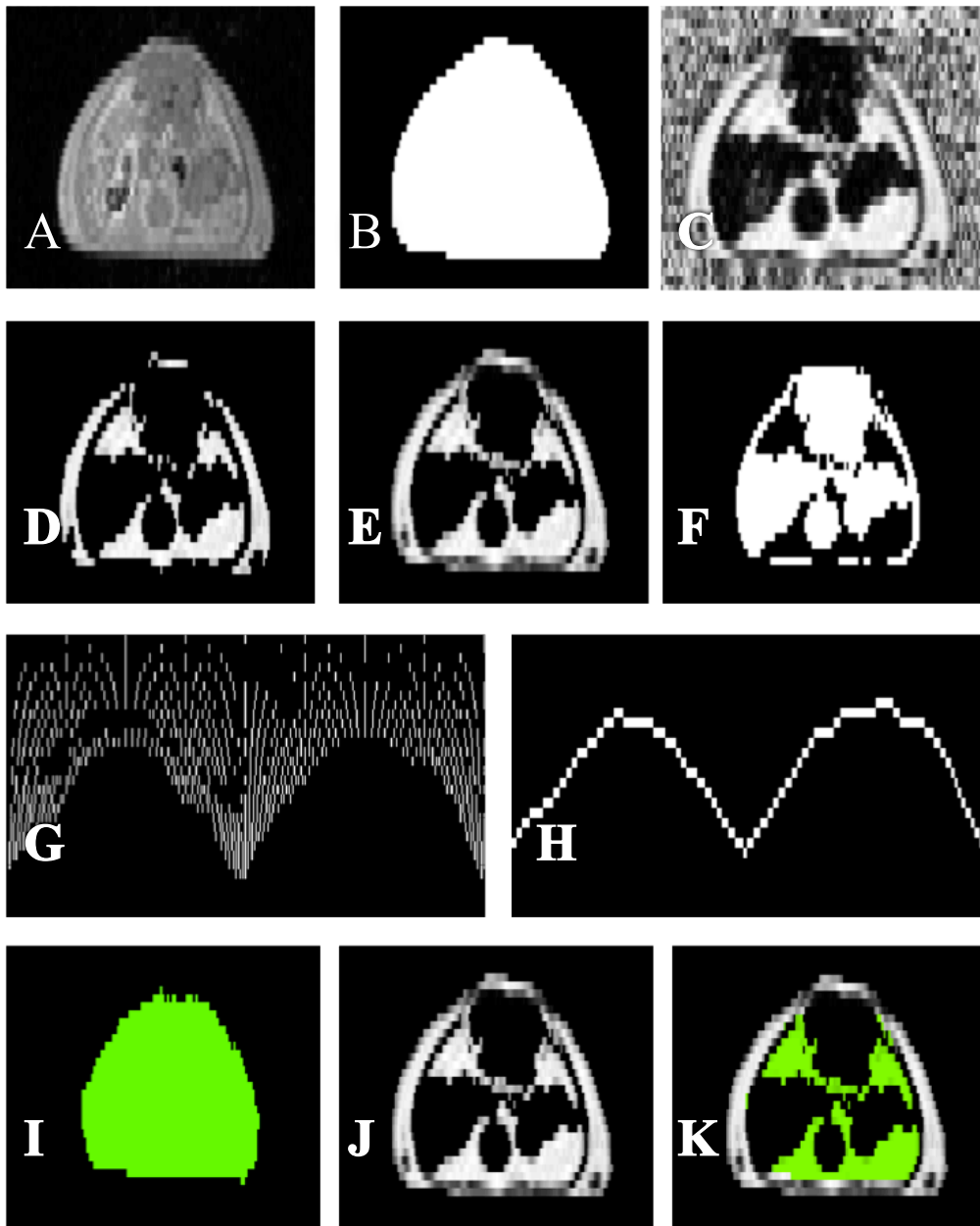


Figure 2.8 Summary of Segmentation Process

The same axial slice is used in all images. A k-means algorithm is applied to the in phase image (A) to create a tissue mask (B). This tissue mask is then applied to the fat fraction image (C). A threshold is then applied to the masked fat fraction image creating a high-fat content image (D). Nearby fat voxels with PVE are then added to create the Total Adipose Mask (E). A threshold is then applied to the masked fat fraction image to create a water image (F). This water image is converted to polar

coordinates (G), and a line is smoothed along the lowest pixels (H). After filling above this line, the image is converted back to Cartesian coordinates to create the abdominal cavity mask (I). This mask is then applied to the total adipose image (J) to separate the IAAT from the SAT.

2.2.3 Segmentation Analysis

The automated segmentation was compared to manual segmentation⁵⁷ (performed with ImageJ software) of 10 equally spaced slices across each animal. Manual segmentation was performed on the same fat-only IDEAL images used in the automated segmentation. Images were manually segmented through use of thresholds on the intensity images to remove low intensity sections and noise. Once a suitable threshold for fat was determined, a binary image was saved as the total adipose tissue. Thresholds used were dependent on the individual slice and not fixed across image sets. Then, the SAT deposit was manually removed from the total adipose mask and saved as the SAT mask. The IAAT mask was then created through a subtraction from the TAT mask. Masks were converted to volumes and compared slice-by-slice with the automated segmentation. The processing time was calculated for both methods.

2.2.4 Reproducibility

Three lean mice were scanned twice on the same day to determine automated segmentation reproducibility. One IDEAL scan was performed on an anesthetized mouse, then the mouse was removed from the scanner, repositioned, and placed back into the scanner and another IDEAL scan was performed. All scans had the same parameters with minor adjustments to FOV positioning if needed. Total volumes of the fat deposits were compared between the automated segmentations.

2.2.5 Statistical Analysis

To compare the automated and manual segmentation methods, slices were compared between the automated and manual methods by first determining the absolute volume

difference (VD_A). VD_A is defined as the absolute difference between the automated (A) and manual (M) volumes, divided by the manual volume shown in Equation 2.1. A VD_A equal to zero shows that both automated and manual methods agreed in the volume of the slice.

Equation 2.1

$$VD_A = |A - M| / M$$

Bland-Altman plots⁵⁸ were also used to visualize the agreement between the two methods. Here, a mean not equal to zero results from a bias between the two methods. For example, a positive mean results from the manual segmentation consistently measuring more fat volume per slice than the automated segmentation. In addition, a small standard deviation between the points will mean that there is greater agreement between the two methods. A slope in the points would correspond to a change in the difference between the techniques at different levels of fat. This is undesirable as a bigger difference between the methods would likely be due to the automated segmentation performing better only at certain levels of fat.

Bland-Altman plots exclusively show volume differences and do not account for shape and location of segmentations. Thus, an additional metric to measure the overlap of the segmented images is required. Here we use the Dice Coefficient (DC)⁵⁹. A perfect overlap of segmentations would be equal to a DC of 1, and can be likened to a 100% match. The DC is calculated with Equation 2.2 by dividing the number of overlapping points (n_{xy}) by the sum of points in the manual segmentation (n_x) and automated segmentation (n_y).

Equation 2.2

$$DC = 2 \cdot n_{xy} / (n_x + n_y)$$

Reproducibility was measured using the coefficient of variation (CV) calculation in Equation 2.3. It is determined with the standard deviation of the absolute differences (σ) and the mean volume measured (μ). Equation 2.3

$$CV = \sigma/\mu$$

Results

Two datasets of obese mice were discarded due to insufficient resolution for segmentation (0.85 x 0.9 mm) in the abdomen near the hips. One lean mouse data set was discarded due to insufficient SNR. All other automated segmentations completed full volumes successfully. The automated technique required 0.6 seconds per slice, whereas manual segmentation required 11 minutes per slice. Full volumetric analysis (70-90 slices) was 50 seconds for the automated segmentation, and over 6 hours for manual segmentation.

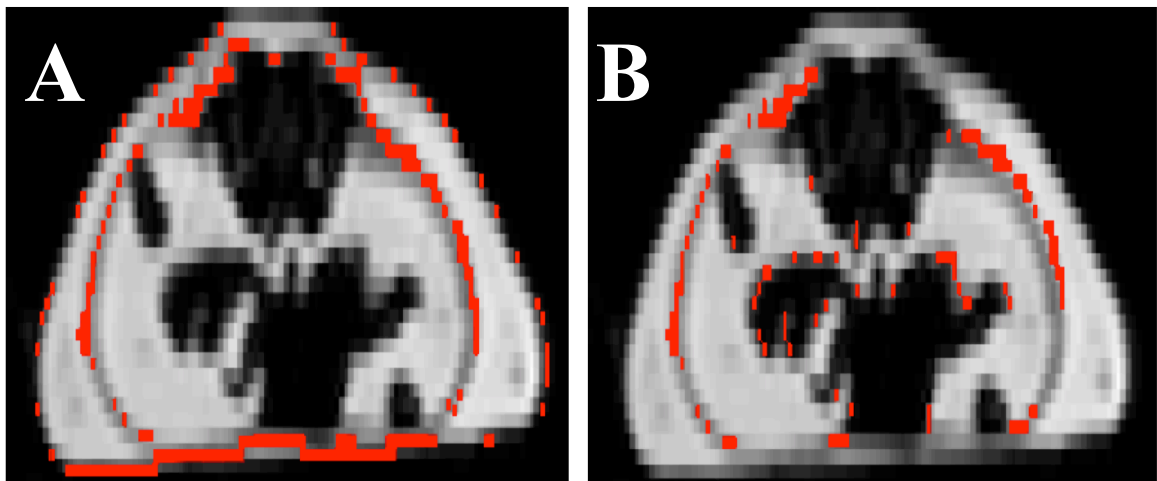


Figure 2.9 Difference Image Between Manual and Automated Segmentations

Lower abdominal axial slice in an obese mouse is depicted. Red voxels show disagreement between the manual and automated segmentations for what is classified as SAT (A) or IAAT (B). The lower abdomen with the highest amount of IAAT is typically the most difficult to segment, and shown here the only disagreements are on edge pixels.

The measured VD_A for SAT was $(6 \pm 5) \text{ mm}^3$ and for IAAT it was $(5 \pm 4) \text{ mm}^3$. Total adipose tissue VD_A was $(12 \pm 6) \text{ mm}^3$. A difference image is shown in Figure 2.9. This relates to the Bland-Altman plots where the mean measured adipose volumes were -2.6

mm^3 for SAT, and 3.1 mm^3 for IAAT. The 95% confidence interval was 21.4 mm^3 for SAT, and 17.6 mm^3 for IAAT. See Figure 2.10 and Figure 2.11 for the plots. The measured Dice coefficients were 0.84 for SAT, and 0.87 for IAAT. The average measured volume for TAT was 116.9 mm^3 per slice, with SAT averaging 55.0 mm^3 per slice and IAAT averaging 61.9 mm^3 per slice.

Coefficients of variation between the repeated tests were 1.8% for IAAT and 1.8% for SAT. Between the two repeated scans, the IAAT was different by an average of 3.57% and the SAT differed by an average of 4.12%.

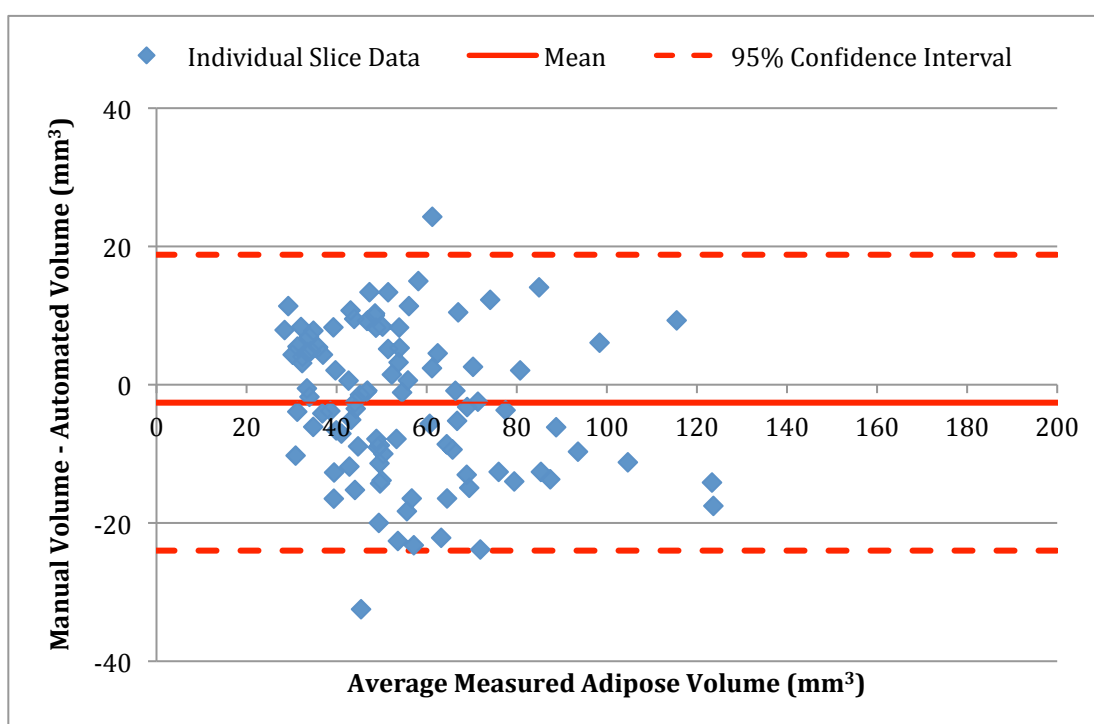


Figure 2.10 Bland-Altman Plot for Subcutaneous Adipose Measurements

Bland-Altman plot of single slice data from measurements using the automated segmentation technique and the manual segmentation technique. Note that the average is below zero meaning that the automated technique tended to measure slightly more subcutaneous adipose than the manual technique.

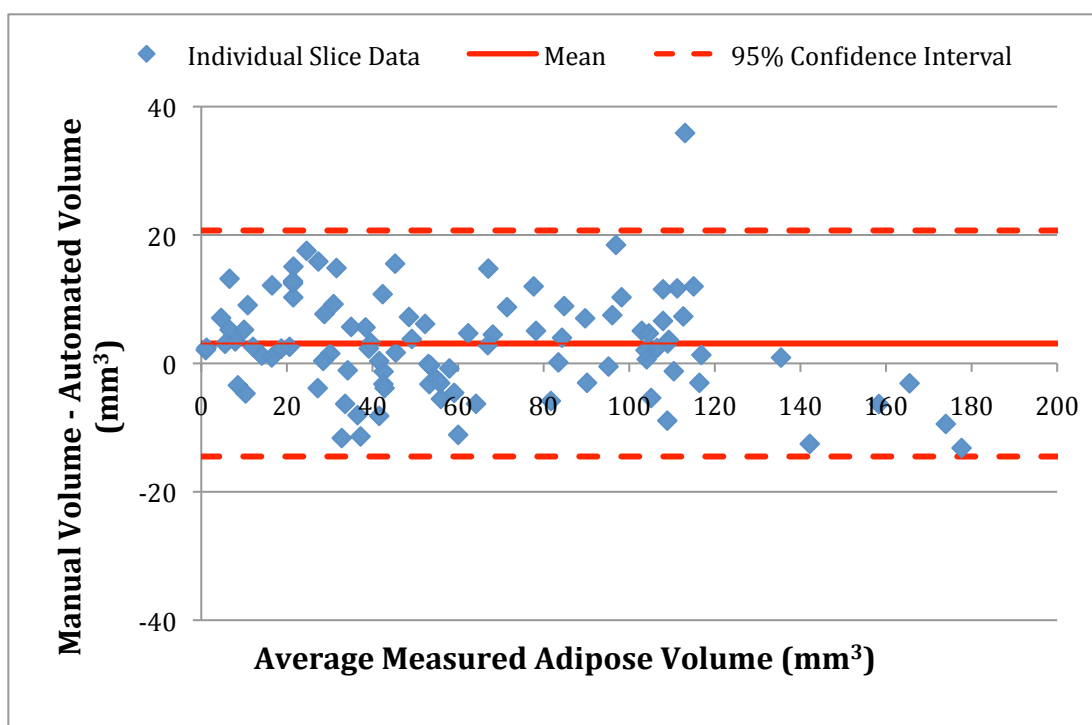


Figure 2.11 Bland-Altman Plot for Intra-Abdominal Adipose Measurements

Bland-Altman plot of single slice data from measurements using the automated segmentation technique and the manual segmentation technique. Note that the average is above zero meaning that the automated technique tended to measure slightly less intra-abdominal adipose than the manual technique. One outlier is present due to the manual technique misclassifying the liver as adipose tissue.

2.3 Discussion

We have demonstrated that a version of AdipoQuant adapted to mouse MRI is able to automatically segment IAAT from SAT in MRI of mice with high agreement to manual segmentations. Less resolution increases the partial volume effects creating more ambiguity for manual segmentation. This ambiguity increases the difficulty of manual segmentation as well as the time required. This is normally a trade-off for the ease of using a clinical scanner, such as a 3T MRI. However, our automated technique was over 300x faster than the manual method resulting in extremely rapid, full volume results (less than 1 min, or 0.6 seconds per slice). No previous training is required to run the

segmentation algorithm. On the other hand, manual segmentation requires enough training for the operator to distinguish anatomy such as the liver as well as training with the manual segmentation software. Thus this technique allows segmentation of mouse images, including those acquired on a clinical MRI system, to be performed without the tradeoff of a longer time investment to analyze and segment the images.

Although other techniques may have comparable automated segmentation times (less than 1 min – 3 minutes), they suffer from other difficulties such as using T1 weighted images for analysis. Automated analyses of T1 weighted images are less robust to image intensity changes resulting from hardware changes (e.g. a change in the coil used for image acquisition), whereas Proton Density Fat Fraction (PDFF) images such as those acquired from IDEAL⁶⁰ are immune to intensity changes caused by switching acquisition hardware. T1 weighted images also have an overlap in intensity values for the liver and the adipose tissue^{26,54,61}. Typically, areas within the bowels are easily mistaken for adipose tissue in T1 weighted images. Water-fat imaging, such as IDEAL, is the superior technique for reproducibly locating adipose tissue⁵⁷. Additionally, unlike other automated analysis methods, the original AdipoQuant technique has already been successfully applied to images from multiple facilities using different hardware and pulse sequences for data acquisition²⁹, demonstrating the algorithm's flexibility.

We suggest a minimum resolution of 0.7 mm axial in-plane resolution for image acquisition. The size of the mouse and the amount of fat in the lower abdominal region dictates how well the algorithm can perform the segmentation. Mice with high IAAT volumes are more difficult to segment in the abdomen near the hips and the largest pixel size that accounted for this was 0.7 mm x 0.7 mm in the axial plane. This was due to the extremely small amount of water between the SAT and IAAT near the hips. If the pixel size was too large it contained high amounts of fat tissue relative to the water tissue. With pixel size at 0.7 mm the voxels over the muscle layer were below 65% fat fraction and thus were distinguishable. As the segmentations were performed in the axial plane, slice thickness was not as important for proper segmentation.

While all segmentations are susceptible to artefacts, our method has additional difficulty with artefacts in the water images. Artefacts in the fat images will only alter the total fat calculated, but artefacts in the water images can cause significant problems in the selection of the abdominal cavity. This only occurs if the water artefact is attached to the water muscle layer and located within the subcutaneous adipose tissue. The further the artefact extends through the subcutaneous adipose tissue, the more problematic the result. The minimal effect is swapping of classification of IAAT and SAT. If the artefact protrudes outside of the subcutaneous adipose tissue, entire sections of SAT will be misclassified causing very high segmentation error. Most notably, phase wrapping of water-based heating apparatuses can cause major issues with segmentation of the IAAT. Utilization of increased image field of view or phase oversampling can eliminate these artefacts, but at the cost of additional scan time. Alternatively, heating apparatuses that do not require water near the animal could also avoid these artefacts.

While manual segmentation was used as a reference standard to for comparison to the automated segmentation, it is far from a perfect technique. It suffers from tediousness, the necessity for training for proper use, and inter-operator and intra-operator differences. In addition, the manual segmentation was performed on the fat-only images that are affected by intensity variation. While not as consistent as using the fat fraction images, it has been validated as an improvement from segmenting T1 weighted images⁵⁷. As T1 weighted segmentation has been validated by comparison to weighing internal organs⁵³, manual segmentation was a validated method for quantifying internal fat and the best choice for comparison of the automated segmentation. Thus, differences depicted in the Bland-Altman plot could be partially or wholly due to erroneous manual segmentation from operator error or intensity variation. This reduces the ability of manual segmentation to determine how well the automated segmentation performs at measuring adipose tissue.

Automated selection of the start and end slices (diaphragm and hips) is a future improvement for this algorithm. Other techniques use water and fat content maps⁵² to alter the segmentation method for specific areas in the mouse. For our method, the start location could be determined automatically as a slice nearby the global maximum of water tissue (lungs / liver). The end location could then be selected as a slice near the

local water maximum posterior to the global fat maximum (legs will create an increase in water in that slice). These fat and water maps could also improve superficial fascia removal from the water masks.

The algorithm was originally adapted from AdipoQuant with significant modifications that accounted for the smaller size and differences in mouse anatomy. These imaging and post processing methods can generally be applied directly to human research, aside from a few changes such as FOV. It is also important that this code works on at clinically relevant MRI strength as this allows the technique to be applied in the same environment, with the same acquisition sequence on mice as it could be with the human technique. This is important in advancing our ability to learn from the mouse models of obesity and their associated diseases to human disease.

Reproducibility results showed that there is high precision between segmentation methods. This allows better research to be performed on longitudinal research, as smaller changes in fat distribution will be observable with this technique, where with manual segmentation the changes could be overshadowed by operator error. In addition, the short analysis time simplifies larger studies allowing more conclusive research.

2.4 Conclusion

In conclusion, we have developed a rapid, repeatable, and automated tool for analyzing fat deposits in mouse MRI. It is over 300 times faster than manual segmentation, is competitive with the leading automated mouse segmentation times, and uses robust quantitative images for more accurate analysis. Unlike other techniques, our technique is usable on low-resolution images. The adaptation of AdipoQuant also allows translation of our technique to human studies. Lastly, the close agreement with manual segmentation shows that this technique is a promising method for advancing our knowledge of obesity through the use of mouse models.

3 Conclusion

3.1 Summary of Findings

This thesis shows the relationship between my automated segmentation technique and manual segmentation. This section summarizes different advantages to using my technique over currently existing techniques for segmentation on rodent MRI. In addition, these advantages are related to the original goal of developing a rapid, reproducible, and transferrable method of segmentation for mouse MRI.

3.1.1 Rapid Analysis of Full Abdominal Volumes

The main advantage to my method over manual segmentation is the large benefit from reduction in time required for analysis. In segmentations of full 80 slice volumes of rodents, the automated segmentation was over 300 times faster. This was due to the requirement of ~6-11 min per slice for manual segmentation, dependent on the difficulty of the slice. In addition, this time cost was increased due to the need for training of new operators. As discussed previously, this includes training of mouse anatomy, identification of anatomy on fat only MR images, and training on the software for analysis (typically ImageJ). The high time cost reduces the ability to analyze a large number of subjects typical in rodent research. With this automated technique lowering time costs to less than one second per slice, full analysis of a large number of subjects becomes trivial because analysis of one subject required 50 seconds for an 80-slice data set. The rate of segmentation was also comparable to other segmentation techniques, with the region growing technique for 9.4 T requiring 40 seconds per full data set, and the segmental shape method requiring 10 seconds per data set. This massive reduction in time compared to manual segmentation opens up more conclusive research by allowing analysis of many more subjects.

3.1.2 Agreement Between Segmentation Techniques

Comparisons of the segmentation techniques using Bland-Altman plots and the Dice coefficient shows very close agreement between the manual and automated

segmentations. The differences could be accounted for by errors in manual segmentation as it is far from a perfect technique. The most important thing to note is that the majority of the differences between the two techniques come from differing classifications around the edges. This is an ambiguous area as classification in manual segmentation is normally at the discretion of the operator; do the volumes of greater than 50% Fat Fraction on voxels containing the muscle layer count as subcutaneous adipose tissue, or do they count as intra-abdominal adipose tissue? This classification has much more consistency when the identification is not based on subjective opinion, but an objective automated method. Bland-Altman results for the competing region growing technique were similar, but unfortunately cannot be accurately compared due to their use of full segmentation results rather than individual slice results. Considering the reduction in time costs and the very similar results between the segmentation methods, the automated segmentation is the superior method.

3.1.3 Reproducibility

A benefit to automation in most segmentation techniques is that the automated method for segmentation usually improves the reproducibility versus manual segmentation. In this case, the extremely low differences in measured fat volumes (3.57% for IAAT, 4.12% for SAT) based on repeated scans showed very high reproducibility. This is vitally important for any studies looking at weight loss or gain over time as variations above 4% in IAAT will be detectable. In comparison to the leading competitors, my automated technique uses fat fraction images over T1 weighted images giving it an advantage in reproducibility.

3.1.4 Transferability

As the segmentation algorithm is based on the AdipoQuant for segmenting human MRI, the ability to transfer techniques and knowledge between mouse and human research is straightforward. Images can be taken with the same MRI scanner, the same acquisition technique (not including changes to the resolution and FOV), and segmented using essentially the same process for both human and mouse images. This is a huge advantage

over other techniques and this is currently the only available technique with this translation ability. The other technique available in both humans and animals, the ATLAS-based technique, uses an entirely different atlas based on the mouse anatomy rather than the human anatomy. My automated segmentation technique is the only existing method that allows direct translation from mouse research to human research.

3.2 Future Work

While my technique has been demonstrated as a powerful and rapid tool for analysis of fat deposits in mice, there are many applications for this tool. The following section will summarize some of these applications, as well as some additions that can be added to optimize the technique.

3.2.1 Disease onset from Obesity

An application of my automated segmentation algorithm that I have already alluded to is investigation of disease onset and its correlation to the distribution of fat content in mice. There is already conclusive evidence that the ratio of IAAT to SAT is highly indicative of disease progression, but determining when disease development begins could be very important for advancing prevention of disease. While the onset and progression of disease in mice could be significantly different than in humans, application of the knowledge gained from mouse models to human research could give important information about diseases. Unlike human studies, mouse models allow strict control of diets and monitoring of progression with increasing obesity. Furthermore, this technique is unique due to its reproducibility and ability to measure very small differences over time.

3.2.2 Expansion to Other Rodents

While mice are the most common laboratory animals for obesity research, other rodent models can provide better information in different areas. A primary example is guinea pigs for their very similar fat development to humans. In addition, rat models are commonly used for research. Both rats and guinea pigs are much larger than mice easing

the resolution to size restrictions that occur with mice. This allows less focus on PVE around the muscle layer so that the main adaptations required for the AdipoQuant algorithm would simply be accounting for the legs or other anatomical differences. My technique could be expanded even further to other animal models but would likely require more in depth work to determine if any differences in anatomy are significant enough to affect segmentation.

3.2.3 Rodent Pregnancy

Another promising area of obesity research is how obesity in pregnancy affects newborns. Early onset diabetes and metabolic syndrome are increasingly problematic in the younger population. Unfortunately, research into human obesity in pregnancy has many levels of difficulty. It is more difficult to get scans without motion when the fetus is included in the image, which is necessary for quantifying abdominal fat deposits. In addition, obese pregnant humans are often too large to fit into conventionally sized MRIs. Using rodent models, this research becomes much simpler. My technique can be used for monitoring the levels of adiposity in pregnant rodents and their fetuses and continuation of monitoring post pregnancy. This could determine the effects of maternal obesity on the offspring.

3.3 Conclusion

My automated segmentation technique has been validated for quantification of adipose tissue in mouse MRI. The comparison to manual segmentation demonstrated that the automated method is a much better technique to use with shorter time costs and similar accuracy. In addition, studies requiring high reproducibility are ideal for the automated technique due to the ability to very small differences between scans in longitudinal studies. My work is an important step towards improving our understanding and management of adiposity through research on mice.

4 References

1. Shields M, Tremblay MS, Laviolette M, Craig CL, Janssen I, Gorber SC. Fitness of Canadian adults: Results from the 2007-2009 Canadian Health Measures Survey. *Health Reports* 2010;21(1).
2. Tjepkema M. Measured Obesity. Adult Obesity in Canada. In: Canada S, editor. Ottawa, Canada; 2005.
3. Corscadden L, Taylor A, Sebold A, Maddocks E, Pearson C. Obesity in Canada: a joint report from the Public Health Agency of Canada and the Canadian Institute for Health Information. Ottawa: Canadian Institute for Health Information, Public Health Agency of Canada; 2011.
4. Ulijaszek SJ. Obesity: preventing and managing the global epidemic. WHO Technical Report Series 894 (pp. 252); 2000; Geneva. World Health Organization. (WHO Technical Report Series 894 (pp. 252)).
5. Sassi F, Devaux M, Cecchini M, Rusticelli E. The Obesity Epidemic: Analysis of Past and Projected Future Trends in Selected OECD Countries: OECD Publishing; 2009. Report nr no.45.
6. Slater J, Green C, Sevenhuysen G, Neil JO, Edginton B. Socio-demographic and geographic analysis of overweight and obesity in Canadian adults using the Canadian Community Health Survey (2005). *Chronic Diseases in Canada* 2009;30(1).
7. Despres JP, Lemieux I, Bergeron J, et al. Abdominal obesity and the metabolic syndrome: Contribution to global cardiometabolic risk. *Arteriosclerosis Thrombosis and Vascular Biology* 2008;28(6):1039-1049.
8. Anis AH, Zhang W, Bansback N, Guh DP, Amarsi Z, Birmingham CL. Obesity and overweight in Canada: an updated cost-of-illness study. *Obesity Reviews* 2010;11(1):31-40.
9. Shi YK, Hu FB. The global implications of diabetes and cancer. *Lancet* 2014;383(9933):1947-1948.
10. Pelletier C, Dai S, Roberts KC, Bienek A, Onysko J, Pelletier L. Diabetes in Canada: facts and figures from a public health perspective. *Chronic Diseases and Injuries in Canada* 2012;33(1):53-54.
11. Isma'eel H, Tellalian D, Hamirani YS, Kadakia J, Nasir K, Budoff MJ. Effect of obesity on coronary artery plaque using 64 slice multidetector cardiac computed tomography angiography. *International Journal of Cardiology* 2010;140(3):358-360.

12. May. Prevalence of Cardiovascular Disease Risk Factors Among US Adolescents, 1999-2008 (vol 129, pg 1035, 2012). *Pediatrics* 2012;130(4):764-764.
13. Despres JP, Lemieux I. Abdominal obesity and metabolic syndrome. *Nature* 2006;444(7121):881-887.
14. Kuk JL, Katzmarzyk PT, Nichaman MZ, Church TS, Blair SN, Ross R. Visceral fat is an independent predictor of all-cause mortality in men. *Obesity* 2006;14(2):336-341.
15. Wajchenberg BL. Subcutaneous and visceral adipose tissue: Their relation to the metabolic syndrome. *Endocr Rev* 2000;21(6):697-738.
16. Bergman RN, Kim SP, Catalano KJ, et al. Why visceral fat is bad: mechanisms of the metabolic syndrome. *Obesity (Silver Spring, Md)* 2006;14 Suppl 1(2S):16S-19S.
17. Weltman A, Weltman JY, Bouchard C, et al. Impact of abdominal visceral fat, growth hormone, fitness, and insulin on lipids and lipoproteins in older adults. *Metabolism* 2003;52(1):73-80.
18. Ross R. Advances in the application of imaging methods in applied and clinical physiology. *Acta Diabetologica* 2003;40:S45-S50.
19. Donato KA, Pi-Sunyer FX, Becker DM, et al. Executive summary of the clinical guidelines on the identification, evaluation, and treatment of overweight and obesity in adults. *Archives of Internal Medicine* 1998;158(17):1855-1867.
20. Romero-Corral A, Somers VK, Sierra-Johnson J, et al. Accuracy of body mass index in diagnosing obesity in the adult general population. *International Journal of Obesity* 2008;32(6):959-966.
21. Price GM, Uauy R, Breeze E, Bulpitt CJ, Fletcher AE. Weight, shape, and mortality risk in older persons: elevated waist-hip ratio, not high body mass index, is associated with a greater risk of death. *American Journal of Clinical Nutrition* 2006;84(2):449-460.
22. Dobbelsteyn CJ, Joffres MR, MacLean DR, Flowerdew G, Res CHHS. A comparative evaluation of waist circumference, waist-to-hip ratio and body mass index as indicators of cardiovascular risk factors. The Canadian Heart Health Surveys. *International Journal of Obesity* 2001;25(5):652-661.
23. Kuk JL, Church TS, Blair SN, Ross R. Does measurement site for visceral and abdominal subcutaneous adipose tissue alter associations with the metabolic syndrome? *Diabetes Care* 2006;29(3):679-684.

24. Shen W, Punyanitya M, Chen J, et al. Visceral adipose tissue: relationships between single slice areas at different locations and obesity-related health risks. *International Journal of Obesity* 2007;31(5):763-769.
25. Abate N, Garg A, Coleman R, Grundy SM, Peshock RM. Prediction of total subcutaneous abdominal, intraperitoneal, and retroperitoneal adipose tissue masses in men by a single axial magnetic resonance imaging slice. *American Journal of Clinical Nutrition* 1997;65(2):403-408.
26. Thomas EL, Saeed N, Hajnal JV, et al. Magnetic resonance imaging of total body fat. *Journal of Applied Physiology* 1998;85(5):1778-1785.
27. Shen W, Chen J, Gantz M, Velasquez G, Punyanitya M, Heymsfield SB. A single MRI slice does not accurately predict visceral and subcutaneous adipose tissue changes during weight loss. *Obesity (Silver Spring, Md)* 2012;20(12):2458-2463.
28. Thomas EL, Bell JD. Influence of undersampling on magnetic resonance imaging measurements of intra-abdominal adipose tissue. *International Journal of Obesity* 2003;27(2):211-218.
29. Addeman BT, Kutty S, Perkins TG, et al. Validation of volumetric and single-slice MRI adipose analysis using a novel fully automated segmentation method. *Journal of Magnetic Resonance Imaging* 2014.
30. Reeder SB, McKenzie CA, Pineda AR, et al. Water-fat separation with IDEAL gradient-echo imaging. *Journal of Magnetic Resonance Imaging* 2007;25(3):644-652.
31. Eggers H, Brendel B, Duijndam A, Herigault G. Dual-Echo Dixon Imaging with Flexible Choice of Echo Times. *Magnetic Resonance in Medicine* 2011;65(1):96-107.
32. Positano V, Gastaldelli A, Sironi AM, Santarelli MF, Lombardi M, Landini L. An accurate and robust method for unsupervised assessment of abdominal fat by MRI. *Journal of Magnetic Resonance Imaging* 2004;20(4):684-689.
33. Kullberg J, Ahlstrom H, Johansson L, Frimmel H. Automated and reproducible segmentation of visceral and subcutaneous adipose tissue from abdominal MRI. *International Journal of Obesity* 2007;31(12):1806-1817.
34. Liou TH, Chan WP, Pan LC, Lin PW, Chou P, Chen CH. Fully automated large-scale assessment of visceral and subcutaneous abdominal adipose tissue by magnetic resonance imaging. *International Journal of Obesity* 2006;30(5):844-852.
35. Wang C-Y, Liao JK. A mouse model of diet-induced obesity and insulin resistance. 2012 2012; United States. p 421-433.

36. Vickers SP, Jackson HC, Cheetham SC. The utility of animal models to evaluate novel anti-obesity agents. *British Journal of Pharmacology* 2011;164(4):1248-1262.
37. Foster MA. *Magnetic resonance in medicine and biology*. Oxford ; New York: Pergamon Press; 1984.
38. Haynes WM, Bruno TJ, Lide DR. *CRC Handbook of Chemistry and Physics*, 95th ed. (pp. 1.13-1.16). Cleveland, Ohio: Chemical Rubber Company; 2014.
39. Haacke EM. *Magnetic resonance imaging: physical principles and sequence design*. (pp. 23-26). New York: J. Wiley-Liss; 1999.
40. Haacke EM. *Magnetic resonance imaging: physical principles and sequence design*. (pp. 84-85). New York: J. Wiley-Liss; 1999.
41. Haacke EM. *Magnetic resonance imaging: physical principles and sequence design*. (pp. 35-47). New York: J. Wiley-Liss; 1999.
42. Haacke EM. *Magnetic resonance imaging: physical principles and sequence design*. (pp. 51-62). New York: J. Wiley-Liss; 1999.
43. Haacke EM. *Magnetic resonance imaging: physical principles and sequence design*. (pp. 111-138). New York: J. Wiley-Liss; 1999.
44. Haacke EM. *Magnetic resonance imaging: physical principles and sequence design*. (pp. 139-162). New York: J. Wiley-Liss; 1999.
45. Haacke EM. *Magnetic resonance imaging: physical principles and sequence design*. (pp. 331-378). New York: J. Wiley-Liss; 1999.
46. Dixon WT. Simple proton spectroscopic imaging. *Radiology* 1984;153(1):189-194.
47. Glover GH. Multipoint Dixon Technique for Water and Fat Proton and Susceptibility Imaging. *Jmri-Journal of Magnetic Resonance Imaging* 1991;1(5):521-530.
48. Glover GH, Schneider E. 3-Point Dixon Technique for True Water Fat Decomposition with B₀ Inhomogeneity Correction. *Magnetic Resonance in Medicine* 1991;18(2):371-383.
49. Reeder SB, Pineda AR, Wen Z, et al. Iterative decomposition of water and fat with echo asymmetry and least-squares estimation (IDEAL): Application with fast spin-echo imaging. *Magnetic Resonance in Medicine* 2005;54(3):636-644.

50. Yu HZ, McKenzie CA, Shimakawa A, et al. Multiecho reconstruction for simultaneous water-fat decomposition and T2*estimation. *Journal of Magnetic Resonance Imaging* 2007;26(4):1153-1161.
51. Judex S, Luu YK, Ozcivici E, Adler B, Lublinsky S, Rubin CT. Quantification of adiposity in small rodents using micro-CT. *Methods* 2010;50(1):14-19.
52. Ranefall P, Bidar AW, Hockings PD. Automatic Segmentation of Intra-abdominal and Subcutaneous Adipose Tissue in 3D Whole Mouse MRI. *Journal of Magnetic Resonance Imaging* 2009;30(3):554-560.
53. Abate N, Burns D, Peshock RM, Garg A, Grundy SM. Estimation of Adipose-Tissue Mass by Magnetic-Resonance-Imaging - Validation against Dissection in Human Cadavers. *Journal of Lipid Research* 1994;35(8):1490-1496.
54. Kullberg J, Angelhed JE, Lonn L, et al. Whole-body T1 mapping improves the definition of adipose tissue: Consequences for automated image analysis. *Journal of Magnetic Resonance Imaging* 2006;24(2):394-401.
55. Tang Y, Sharma P, Nelson MD, Simerly R, Moats RA. Automatic Abdominal Fat Assessment in Obese Mice Using a Segmental Shape Model. *Journal of Magnetic Resonance Imaging* 2011;34(4):866-873.
56. Casanueva FF, Moreno B, Rodríguez-Azaredo R, et al. Relationship of abdominal obesity with cardiovascular disease, diabetes and hyperlipidaemia in Spain. *Clinical Endocrinology* 2010;73(1):35-40.
57. Alabousi A, Al-Attar S, Joy TR, Hegele RA, McKenzie CA. Evaluation of Adipose Tissue Volume Quantification With IDEAL Fat-Water Separation. *Journal of Magnetic Resonance Imaging* 2011;34(2):474-479.
58. Bland JM, Altman DG. Statistical Methods for Assessing Agreement between Two Methods of Clinical Measurement. *Lancet* 1986;1(8476):307-310.
59. Dice LR. Measures of the Amount of Ecologic Association between Species. *Ecology* 1945;26(3):297-302.
60. Reeder SB, Hu HCH, Sirlin CB. Proton density fat-fraction: A standardized mr-based biomarker of tissue fat concentration. *Journal of Magnetic Resonance Imaging* 2012;36(5):1011-1014.
61. Brennan DD, Whelan PF, Robinson K, et al. Rapid automated measurement of body fat distribution from whole-body MRI. *American Journal of Roentgenology* 2005;185(2):418-423.

5 Ethics Approval



AUP Number: 2011-055

PI Name: McKenzie, Charles

AUP Title: Molecular and Metabolic MRI of Non-Alcoholic Fatty Liver Disease

Approval Date: 11/15/2011

Official Notice of Animal Use Subcommittee (AUS) Approval: Your new Animal Use Protocol (AUP) entitled "Molecular and Metabolic MRI of Non-Alcoholic Fatty Liver Disease" has been APPROVED by the Animal Use Subcommittee of the University Council on Animal Care. This approval, although valid for four years, and is subject to annual Protocol Renewal.2011-055::1

1. This AUP number must be indicated when ordering animals for this project.
2. Animals for other projects may not be ordered under this AUP number.
3. Purchases of animals other than through this system must be cleared through the ACVS office. Health certificates will be required.

The holder of this Animal Use Protocol is responsible to ensure that all associated safety components (biosafety, radiation safety, general laboratory safety) comply with institutional safety standards and have received all necessary approvals. Please consult directly with your institutional safety officers.

Submitted by: Copeman, Laura
on behalf of the Animal Use Subcommittee
University Council on Animal Care

6 Curriculum Vitae

Colin M McCurdy

ACADEMIC INFORMATION

- | | |
|---------------|---|
| 09/12 – 08/14 | <p>Candidate for M.Sc. in Medical Biophysics</p> <p>The University of Western Ontario, London, ON</p> |
| 09/07 – 02/12 | <p>B.Sc. in Honours Co-op Biophysics</p> <p>University of Guelph, Guelph, ON</p> |
-

RESEARCH EXPERIENCE

- | | |
|-----------------|--|
| 09/12 - Present | <p>Graduate Studies</p> <p>Dr. Charles McKenzie</p> <p>The University of Western Ontario, London ON</p> <p>Project Focus: Advancing techniques that allow the automated quantification of visceral fat in human Magnetic Resonance (MR) images to use on mouse images.</p> <ul style="list-style-type: none"> • Editing and creating code in MATLAB • Imaging mice on MRI • Validation of fat quantification in mice through comparison to manual segmentation |
|-----------------|--|

RESEARCH EXPERIENCE

05/11 – 08/11

Student Assistant

Dr. Charles McKenzie

The University of Western Ontario, London ON

Project Focus: To implement and optimize a combination of MR image reconstruction techniques (Parallel MR Imaging and Compressed Sensing) to improve patient scan times.

- Implemented the l1-SPIRiT reconstruction technique for use on under sampled MR images
- Coded a function in C to allow image data collection as a poisson disk sampling distribution for optimal reconstruction with the l1-SPIRiT
- Developed a GUI in MATLAB for use of image reconstruction methods

PUBLICATIONS

Wiens CN, **McCurdy CM**, Willig-Onwuachi JD, McKenzie CA, R2*-corrected water-fat imaging using compressed sensing and parallel imaging. *Magnetic Resonance in Medicine*, 2013.

Addeman BT, Kutty S, Perkins TG, Soliman AS, Wiens CN, **McCurdy CM**, Beaton MD, Hegele RA, McKenzie CA, Validation of Volumetric and Single Slice MRI Adipose analysis using a novel Fully Automated Segmentation method. *Journal of Magnetic Resonance Imaging*, 2014.

PRESENTATIONS

Oral Presentations

Friesen-Waldner LJ, Wade TP, Wiens CN, Harris JK, Sinclair KJ, **McCurdy CM**, Chen A, McKenzie CA, Imaging of Brown Fat Metabolism Using Hyperpolarised Carbon-13 MRI. *Exploring the Role of Brown Fat in Humans*. Bethesda, Maryland, 2014.

Wiens CN, **McCurdy CM**, McKenzie CA, A combined approach to Compressed Sensing and Parallel Imaging for Fat-Water Separation with R2* estimation. *Proceedings of the 20th Annual Meeting of ISMRM*. Melbourne, Australia, 2012 (Abstract 0007).

Poster Presentations

McCurdy CM, Addeman BT, Wiens CN, Friesen-Waldner LJ, Wade TP, Harris JK, Sinclair KJ, McKenzie CA, Fully Automated Volumetric Adipose Tissue Quantification in Magnetic Resonance Images of Mice. *International Society of Magnetic Resonance in Medicine*. Milan, Italy, 2014 (Abstract 2145)

McCurdy CM, Addeman BT, Wiens CN, Friesen-Waldner LJ, Wade TP, Harris JK, Sinclair KJ, McKenzie CA, Feasibility of Fully Automated Volumetric Adipose Tissue Quantification in Magnetic Resonance Images of Mice. *Exploring the Role of Brown Fat in Humans*. Bethesda, Maryland, 2014.

McCurdy CM, Addeman BT, Wiens CN, Friesen-Waldner LJ, Wade TP, Harris JK, Sinclair KJ, McKenzie CA, Feasibility of Fully Automated Volumetric Adipose Tissue Quantification in Mice. *London Imaging Discovery Forum*. London, Ontario, 2013
(Abstract Accepted)

Sinclair KJ, Friesen-Waldner LJ, **McCurdy CM**, Wiens CN, Wade TP, de Vrijer B, Regnault TRH, McKenzie CA, Quantification of total adipose tissue in fetal guinea pigs subjected to suboptimal in utero conditions using water-fat MR. *International Society of Magnetic Resonance in Medicine*. Milan, Italy, 2014 (Abstract 3031)

Harris JK, Gibson E, Hamilton A, **McCurdy CM**, Friesen-Waldner LJ, Ward AD, McKenzie CA, Feasibility of Brown Adipose Tissue Histology and 3D Whole Mouse MRI Co-registration. *Exploring the Role of Brown Fat in Humans*. Bethesda, Maryland, 2014.

Sinclair KJ, Friesen-Waldner LJ, **McCurdy CM**, Wiens CN, Wade TP, Regnault TRH, McKenzie CA, Detection of brown adipose tissue in guinea pig fetuses using MRI. *Exploring the Role of Brown Fat in Humans*. Bethesda, Maryland, 2014.

Friesen-Waldner LJ, Wade TP, Wiens CN, Harris JK, Sinclair KJ, **McCurdy CM**, Chen A, McKenzie CA, Imaging of Brown Fat Metabolism Using Hyperpolarised Carbon-13 MRI. *Exploring the Role of Brown Fat in Humans*. Bethesda, Maryland, 2014.

Wiens CN, **McCurdy CM**, McKenzie CA, R2*-correct Fat-Water Imaging using Compressed Sensing and Parallel Imaging. *Fat-Water Separation Workshop*. Long Beach, USA, 2012 (Abstract 28).

SCHOLARSHIPS & AWARDS

- | | |
|---------------|--|
| 09/11 - 12/11 | Western Graduate Research Scholarship <ul style="list-style-type: none">• \$ 4,500 for 1 year of Graduate Studies• Requires above 78% average for each year awarded |
| 09/10 - 12/10 | SC Johnson Sons and Daughters Scholarship <ul style="list-style-type: none">• \$ 14,000 over 4 years for undergraduate degree• Awarded based on scholastic attainment, leadership qualities, character, community service and diversity of interest |

PROGRAMMING SKILLS

- MATLAB
- C and C++
- Java